REPORT DOCUMENTATION PAGE

Form Approved
OMB No. 0704-0188

PLEASE DO NOT RETURN YOUR FORM TO THE ABOVE ADDRESS.

1. REPORT DATE *(DD-MM-YYYY)*	2. REPORT TYPE	3. DATES COVERED *(From - To)*
05-31-2011	Final Technical	03-01-2010 to 02-28-2011

4. TITLE AND SUBTITLE

Thrust and Efficiency Performance of the Microcavity Discharge Thruster

5a. CONTRACT NUMBER

5b. GRANT NUMBER

FA9550-09-1-0161

5c. PROGRAM ELEMENT NUMBER

6. AUTHOR(S)

Burton, Rodney L., Eden, J. Gary, Raja, Laxminarayan L., Park, Sung-Jin, Laystrom-Woodard, Julia, and de Chadenedes, Mark

5d. PROJECT NUMBER

5e. TASK NUMBER

5f. WORK UNIT NUMBER

7. PERFORMING ORGANIZATION NAME(S) AND ADDRESS(ES)

University of Illinois at Urbana-Champaign, Dept. of Aerospace Engineering, 104 S. Wright St., Urbana, IL 61801
University of Texas at Austin, Austin, TX 78712
CU Aerospace, LLC, Champaign, IL 61820

8. PERFORMING ORGANIZATION REPORT NUMBER

UIUC AFOSR Yr. 2 Final Report

9. SPONSORING/MONITORING AGENCY NAME(S) AND ADDRESS(ES)

Air Force Office of Scientific Research
875 North Randolph Street
Suite 325, Rm 3112
Arlington, VA 22203

10. SPONSOR/MONITOR'S ACRONYM(S)

AFOSR

11. SPONSOR/MONITOR'S REPORT NUMBER(S)

AFRL-OSR-VA-TR-2012-0381

12. DISTRIBUTION/AVAILABILITY STATEMENT

Unlimited - A

13. SUPPLEMENTARY NOTES

14. ABSTRACT

This work has focused on the potential of microcavity discharge devices to serve in an electrothermal thruster role, especially in the case of nanosatellite propulsion. An MCD device concentrates a capacitive electric field (~10^7 V/m) inside the cavity, initiating plasma breakdowns, and increasing the propellant gas temperature. MCD thrust tests were performed on a compact thrust stand and indicated that an integral micronozzle produced a thrust coefficient large enough to be effective from an efficiency standpoint. Paschen minimum breakdown tests provided a practical limit on the line pressure used in testing and a rough system-level estimate of the voltages required to make optimal use of the thruster. Heating and thermal efficiency testing indicated the MCD thruster was capable of a high degree of heating and moderate thermal efficiency, up to To = 555 K and 22%. Increased nitrogen content in the propellant gas generally increased the degree of heating and efficiency observed, due to rotational and vibrational excited states, and location of discharge heating away from the cavity walls, reducing wall heat losses and increasing the thermal efficiency.

15. SUBJECT TERMS

microcavity discharge, electrothermal thruster, rf-heated plasma, micronozzle

16. SECURITY CLASSIFICATION OF:			17. LIMITATION OF ABSTRACT	18. NUMBER OF PAGES	19a. NAME OF RESPONSIBLE PERSON
a. REPORT	b. ABSTRACT	c. THIS PAGE			Rodney L. Burton
U	U	U	UU	65	19b. TELEPHONE NUMBER *(Include area code)* 217-244-6223

Executive Summary

Research Results

A new trend in space exploration is the deployment of small-scale satellites known as nanosatellites. Nanosatellites have the potential to be an effective means of performing low-cost research and observation missions, but the lack of an effective, compact, and efficient propulsion system remains an obstacle. This work has focused on the exploration of the potential of microcavity discharge devices to serve in an electrothermal thruster role, especially in the case of nanosatellite propulsion. Microcavity discharge devices represent a new type of electronic device that was originally developed for use in plasma displays. An MCD device is a modified capacitor where one or more microcavities have been formed within each plate and then concentrically aligned to concentrate the capacitive fringe effects and magnify the electric field inside the cavity. MCD devices can be adapted to serve as thrusters by applying an AC voltage, causing the strong electric field inside the cavity to initiate plasma breakdowns, increasing the propellant gas temperature. Development of this electrothermal thruster, named the MCD thruster, has been conducted primarily on an experimental basis with computational modeling support. In order to validate the performance of the MCD thruster three sets of tests have been performed: thrust tests, Paschen minimum breakdown tests, and thermal efficiency tests.

Thrust tests were performed on a compact thrust stand and indicated that an integral micronozzle produced a thrust coefficient large enough to be effective from an efficiency standpoint. Paschen minimum breakdown tests determined that the correct distance to use in the Pd parameter was the linear separation distance between the aluminum substrates of the two electrode foils. This finding differs from MCD devices used for illumination where the cavity diameter is the dominant distance. Paschen testing also provided a practical limit on the line pressure used in testing and a rough system-level estimate of the voltages required to make optimal use of the thruster. Heating and thermal efficiency testing indicated the MCD thruster was capable of a high degree of heating and moderate thermal efficiency, up to 280 K and 22%. Increased nitrogen content in the propellant gas generally increased the degree of heating and efficiency observed, due to two factors. First, in the MCD process nitrogen is a more effective energy absorbing agent, as the energy imparted by a collision is stored in the rotational and vibrational excited states in addition to the electronic excited state, and as a result greater energy is deposited in the propellant gas. Second, the addition of nitrogen to the propellant gas results in the majority of the heating occurring away from the cavity walls, reducing wall heat losses and increasing the thermal efficiency.

Although the current generation of MCD thrusters is limited due to material choices and fabrication processes, they are still capable of a relatively high level of performance. The optimal operating conditions, as determined by the maximum thermal efficiency and the resulting heating and efficiency are found to occur with a mixture of argon-15% nitrogen, for which a constant mass flow rate with heating resulted in a pressure increase of 50 - 75%, and a corresponding stagnation temperature increase of 125 – 200%.

Publications Resulting from Research

Burton R. L. [et al.] Development of the MCD Thruster for Nanosat Propulsion, Proceedings of the 57th Joint Army Navy NASA Air Force Propulsion Meeting. - Colorado Springs, Colorado, 2010.

Burton R. L., et al Initial Development of the Microcavity Discharge Thruster, Proceeding of the 31st Internation Electric Propulsion Conference. - Ann Arbor, Michigan , 2009.

de Chadenedes M. [et al.] Advances in Microcavity Discharge Thruster Technology, Proceedings of the 46th AIAA/ASME/SAE/ASEE Joint Propulsion Conference. - Nashville, TN, 2010.

de Chadenedes M. Propulsion Performance of a Microcavity Discharge Device, Masters Thesis, University of Illinois at Urbana Champaign, Urbana, IL, 2011.

Sitaraman H. and Raja, L. L., "Simulation studies of Alternating-Current Microdischarges for Microthruster Applications," *48th AIAA Aerospace Sciences Meeting*, Jan, 2010, Orlando, FL

Sitaraman H. and Raja L. L., "Simulation studies of micrometer scale dielectric barrier discharges for microthruster applications", *IEEE Conf. on Plasma Science*, June, 2010, Norfolk, VA

Sitaraman H. and Raja L. L., "Two-Dimensional Simulations of Micro Cavity Discharges for Micro-Propulsion Applications", *48th AIAA Aerospace Sciences Meeting*, Jan, 2011, Orlando, FL

Sitaraman H and Raja L. L., "Simulation of RF Microdischarges for Microthruster Applications," *IEEE Transactions on Plasma Science*, (Special Issue on Images in Plasma Science), (in review).

Sitaraman H. and Raja L. L., "Gas temperature effects in micrometer scale dielectric barrier discharges," *Journal of Physics D: Applied Physics*, (in review)

Acknowledgements

This work has been sponsored by the United States Air Force Office of Scientific Research, Grant AF FA9550-09-1-0161. Dr. Mitat Birkan is the Program Manager.

Table of Contents

Nomenclature

η	Efficiency
I_{sp}	Specific impulse
W	Watts
V	Velocity
ΔV	Change in velocity
F	Thrust
t	Time
m	Mass or meters
P	Power
P_p	Propulsive Power
U	Velocity
U_e	Exhaust velocity
ϕ	Power fraction
U_c	Cold exhaust velocity
$\dot{m}$	Mass flow rate
C_p	Isobaric specific heat
T	Temperature
T_o	Stagnation temperature
q	Local wall heat losses
τ_w	Local wall shear stress
f	Friction coefficient
ρ	Density
g	Acceleration due to gravity
Q	Total heat losses
γ	Specific heat ratio
R	Gas constant
Re	Reynolds number
d	Diameter or separation distance
C_f	Thrust Coefficient

1.0 INTRODUCTION

1.1 Requirement for a Compact and Efficient Thruster

A continuing problem in the utilization and development of space-based technologies remains the high costs of launching a payload into orbit. While the commonly accepted figure of approximately $10,000 per pound to Low Earth Orbit (LEO) is not entirely accurate, costs still remain in the range of $2000-$5000/lb (Watts, 2001) with increasing costs for Geosynchronous Earth Orbit (GEO), Geosynchronous Transfer Orbits (GTO), and High Earth Orbit (HEO). Although recent developments in launch vehicle technology have the potential to greatly decrease the cost of delivering a significant payload to orbit, for any small to medium sized institution such costs are still prohibitively high. One way to reduce these costs is simply to launch a very small payload, often in the form of satellites massing less than 10 kg. With the development of the Cube Sat specification (Cubesat Program, 2009) and other similar micro-, nano-, and picosatellite standards (indicating satellites of mass < 100 kg, 10 kg, and 1 kg respectively) new options have emerged for small scale satellite missions. The main advantage of these small satellites is the fact that their low mass allows them to "piggy back" on the launch vehicle of a larger payload, greatly reducing launch costs. In addition, because of their mass and volume restrictions nanosatellites have a relatively simple design, and they can be and often are designed and assembled by teams of university students. Unfortunately while nanosatellites are effective tools for teaching and performing limited-scale science missions, the unavailability of a suitable thruster remains an impediment.

A common limitation encountered in mission planning for nanosatellites is the lack of an efficient and compact propulsion system. Usually, nanosatellites are deployed in LEO or near-LEO and tend to be jettisoned while the launch vehicle transitions to the deployment orbit for its main payload. (Baker, 2005) This can lead to problems with attitude control, orbit stabilization, and even orbit degeneration if the initial deployment goes wrong (for the CubeSat specification, the satellites are launched out of the carrier pod by a compressed spring). Any one of these problems can irreversibly harm a nanosatellite mission if there is no way to correct the situation, which can make satellite deployment a "do-or-die" proposition. In order to fully utilize the potential of and to prolong the usable mission time of a nanosatellite a propulsion system is a necessary component. However, since the size and system capacity of nanosatellites are extremely limited, any propulsion system employed by nanosatellites must be both extremely compact and highly efficient.

1.1.1 Nanosatellite Application

The intended primary application for the MCD thruster is nanosatellites (satellites of mass < 10 kg), such as those designed to the Cube Sat specification. The MCD thruster is especially suited for operation on small satellites for several reasons which will be described later in this section. As with the development of any propulsion system, the performance requirements must first be established.

The question at issue is what range of efficiency and specific impulse are appropriate for a nanosatellite electric micropropulsion system. Currently a number of EP systems

have been successfully deployed including the pulsed plasma thruster (10% η, 1000 s I_{sp}); the resistojet (50%, 300 s); the Hall thruster (50%, 2000 s); and the ion thruster (70%, 3000 s). Other EP systems in advanced development are the colloid thruster (30%, 700 s); and the FEEP thruster (95%, 6000 s). One important note is that since available space and power is extremely limited onboard, nanosatellite propulsion systems have different requirements than the systems typically installed on conventional satellites or spacecraft. This limited power situation is a critical component of nanosatellite propulsion, since it restricts the types of thrusters that may be selected. Due to scaling factors, both electrostatic- and electromagnetic-type thrusters require either much higher constant power levels (ion, Hall effect) than a nanosatellite is capable of providing, or a power storage array, often in the form of capacitors (MPD's), that dwarfs the size never mind the capacity of a nanosatellite. Examples include Warner and Martinez-Sanchez's (Warner, et al., 2006) miniature Hall effect thruster design with a nominal power of 200 W, far in excess of the 5-25 W available on a nanosatellite bus or a power storage array and the gallium electromagnetic (GEM) thruster developed by Thomas at UIUC (Thomas, 2010) which has a capacitor array weighing some 500 lbs. Therefore, the available power supply of a nanosatellite necessarily restricts the choice of an electric propulsion system to electrothermal-type thrusters. A brief summary of currently available small-scale electrothermal thrusters can be seen in Table 1.1.

As noted previously, propulsion selection for nanosatellites depends on the propulsion capability as expressed in terms of the maneuver time and the required orbital maneuver ΔV, as well as on the mass and volume available for the propulsion system on the nanosatellite. Since nanosatellite mass and volume requirements are usually strictly specified, a 1U CubeSat for example has dimensions of 10 x 10 x 10 cm with a mass of 1 kg, they are often inflexible design parameters when dealing with nanosatellite development. Thus the maneuver capability requirements are necessarily the only flexible values in the system design parameter space. The maneuver time requirement is due to the limited lifetime of nanosatellites, and the factors that determine a suitable maneuver time will be dealt with in subsequent sections. The ΔV requirement is conventional in nature, and the necessary magnitude can be found without difficulty.

Table 1.1: Comparison of Electrothermal Thrusters

Thruster Type	Propellant	Efficiency	I_{sp} [s]	Comment
High Power Arcjet	Ammonia	28%	780	26 kW AF ESEX in-space(Fife, et al., 2002)
Low Power Arcjet	Hydrazine	36%	435	500 W. Discharge is unstable, inefficient at low power levels (Lichon, 1997)
Low Power Microwave	Helium	5%	180	14 W, large wall loss (Goovaerts, et al., 2007)
Microwave Microthruster	Argon	9%	80	10 W, large wall loss (Takao, et al., 2007)
High Power Resistojet	N_2, Helium	84%	100-200	300 W, long warm-up (Morren, 1989)
Microresistojet	N_2, Helium	20-40%	100-200	1 W, large heat loss, long warm-up (1968)
Microcavity Discharge	Ne, N_2, Ar	50-70%	100-400	1 W per cavity, small wall loss (Becker, 2006)

The approximate range of specific impulse appropriate for nanosatellite microthrusters is found by writing a simplified version of the equation describing the maneuver time *t* required to achieve a velocity change ΔV, where:

$$\Delta V \sim Ft/m \ \ (\text{Thrust x maneuver time/mass}) \tag{1.1}$$

The ΔV equation is approximate because, for simplicity, the satellite mass m is taken as constant during the maneuver, i.e. only a small mass fraction of fuel is consumed.
The exhaust energy equation is used to define the thrust efficiency η as the ratio of net thrust power to propulsive power P_p:

$$\tfrac{1}{2}\dot{m}U_e^2 = \tfrac{1}{2}TU_e = \eta P_p + \left(\tfrac{1}{2}\dot{m}U_e^2\right)_c \tag{1.2}$$

Here the cold thrust power $\left(\tfrac{1}{2}\dot{m}U_e^2\right)_c = \tfrac{1}{2}T_cU_c$ is the exhaust power without thruster heating. For many electrostatic or electromagnetic propulsions systems including ion thrusters, Hall-effect thrusters, and PPTs the cold thrust power is small or negligible, but for electrothermal thrusters it is approximately independent of thruster heating. The thrust efficiency is then:

$$\eta = \frac{\tfrac{1}{2}\dot{m}U_e^2 - \left(\tfrac{1}{2}\dot{m}U_e^2\right)_c}{P_p} = \frac{\Delta\left(\tfrac{1}{2}\dot{m}U_e^2\right)}{\phi P} \tag{1.3}$$

where ϕ is the power fraction P_p/P, defined in terms of the propulsive power P_p, and the maximum nanosatellite bus power P produced by the solar panels. Typically, $\phi = 0.5$, but $\phi > 1$ is possible with batteries and deployable solar panels.
For a typical electrothermal case where $U_e \approx 2U_c$ (1968) the maneuver time becomes:

$$t \approx \frac{\tfrac{1}{2}\Delta V U_e}{\eta\phi(P/m)} \tag{1.4}$$

This equation for maneuver time t shows that for a given ΔV, reduced maneuver time requires low specific impulse, high efficiency, high power fraction, and high specific power P/m. For a typical rapid response system we have $\eta\phi \approx 0.50$ and $P/m \approx 1\ \text{W/kg}$. (Ghosh, 2009) To summarize:

- For maximum nanosatellite mission capability, it is always desirable to maximize efficiency η, power fraction ϕ, and specific power P⁄m, recognizing that η, ϕ, and P⁄m have limited range.
- For a desired maneuvering capability ΔV, and thrust time t, the specific impulse is determined.

To find the maneuver capability ΔV in terms of specific impulse and maneuver time, the maneuver time equation is rewritten:

$$\Delta V = \frac{2\eta\phi(P/m)t}{U_e} \tag{1.5}$$

This equation, showing that the introduction of a constrained maneuver time gives ΔV varying *inversely* with I_{sp} is counterintuitive, in that high ΔV interplanetary missions are high specific impulse. The conclusion is that, in order to minimize orbit transfer times, more maneuver capability is available for propulsion systems with low exhaust velocity and specific impulse. Insisting incorrectly on a high I_{sp} incurs either a large maneuver time or a limited nanosatellite ΔV capability.

The next logical question is the appropriate maneuver time for a nanosatellite. Since low-cost nanosatellites have a limited design life (~1 year) in a rapid response environment, it is not useful for maneuver times to be on the order of weeks or months given the delayed response, high mission control support costs and long satellite downtimes associated with such durations. It is more reasonable that the time to perform a maneuver should be measured in days. Figure 1.1 shows some typical ranges of ΔV per day as a function of I_{sp} for a maneuverable nanosatellite. It is assumed that $\eta\phi \approx 0.50$, $P/m \approx 1\ \mathrm{W/kg}$, $g \approx 10\ \mathrm{m/s^2}$, and that the desired time for a single maneuver is 1.0 days.

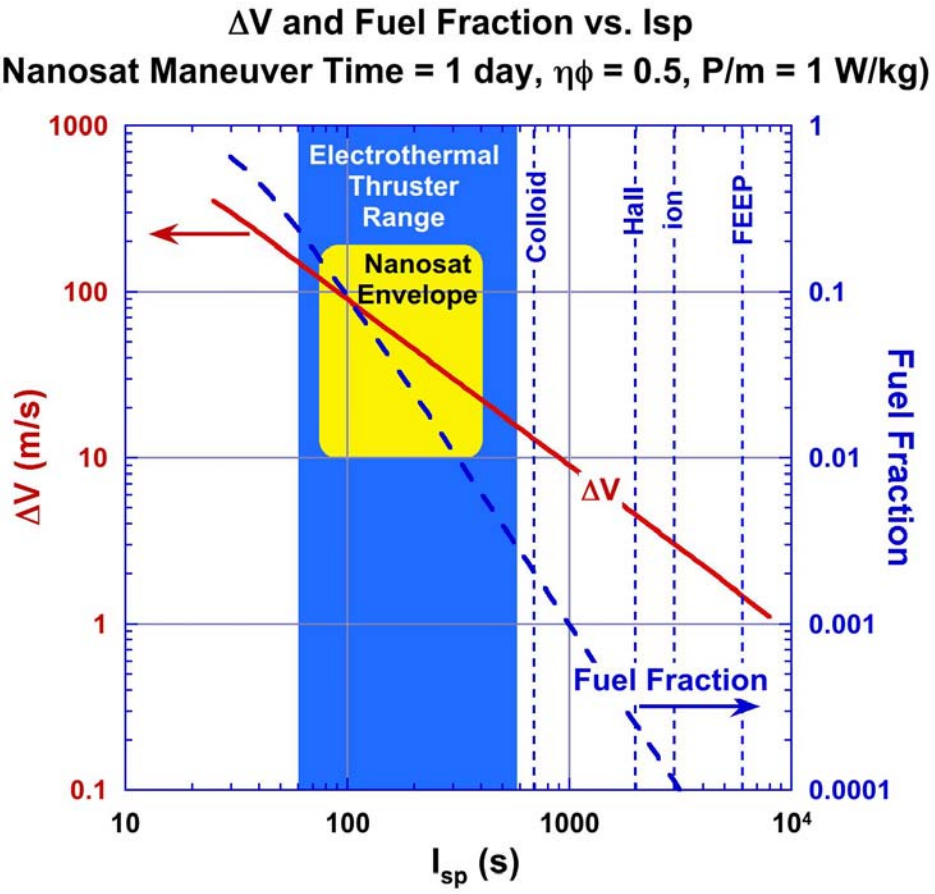

Figure 1.1: Operating envelope for nanosatellite propulsion. Maneuver time is one day, requiring high thrust and reducing specific impulse to the electrothermal range.

From Figure 1.1, the "sweet spot" for nanosatellite orbital maneuvers (shaded region) is in the I_{sp} range of 100 – 400 s, where ΔV is relatively large, but the fuel fraction is reasonably small. For an I_{sp} of 50 s, typical of cold gas thrusters, ΔV is high but the fuel fraction is too large. For I_{sp} > 2000 s, the ΔV per day is too small to be useful in time-constrained maneuvers. The colloid thruster at 700 s and 30% efficiency (Spence, et al., 2008) could eventually be considered assuming significant improvements in efficiency and system volume, but is presently not competitive. Furthermore, it was noted that a nanosatellite propulsion system could operate from batteries. For a 5 kg, 5 W nanosatellite operating for one day, the required energy is 432 kJ = 120 W-hr. Lithium-ion batteries of this size would have a mass of about 1 kg, or 20% of the satellite mass, making battery operation possible. Batteries could be used in conjunction with photovoltaic cells to increase power and decrease maneuver time, effectively providing $\phi > 1$.

Electrothermal thrusters can in principle operate at high efficiency at low I_{sp}. They have no inherent requirement for highly ionized propellant, which can be made sufficiently conductive with an ionization fraction of 10^{-3} – 10^{-6} and are easily designed with nozzles having Reynolds numbers of sufficient magnitudes to avoid excessive wall losses.

Additionally, in their powered state they offer sufficient thrust and I_{sp} gains to compensate for the additional mass and power requirements over traditional cold-gas thrusters (it should also be noted that conventional electrothermal thrusters can serve as cold-gas thrusters should the need arise). Finally, electrothermal thrusters are simple in nature with few complex parts, thus eliminating the need for redundant or over-designed components thereby saving valuable system mass. The combination of these features makes them ideal propulsion systems for nanosatellites: compact, efficient, robust, and with high relative thrust. The study by A. Baker et al (Baker, 2005) gives a number of different mission profiles for low-cost nanosatellites utilizing either cold-gas or low power electrothermal thrusters, giving a good indication of the feasibility of such a mission and confirming electric propulsion as a viable option for nanosatellites.

1.1.1.1 The Microcavity Discharge Thruster

The results of Table 1.1 and equation (1.3) demonstrate that a low power, low I_{sp} electrothermal thruster capable of a relatively high level of thrust can be used to maximize the usable deployment time of a typical nanosatellite. Recent advances in microcavity discharge (MCD) technology have provided a possible candidate for this role in the form of the Microcavity Discharge thruster. (Spence, et al., 2008) The MCD thruster (see Figure 1.2) is an extremely small-scale electrothermal thruster which utilizes a capacitively coupled dielectric barrier plasma discharge as the primary heating mechanism. The fundamental structure of the MCD thruster is two aluminum foils coated in a nanoporous aluminum dioxide dielectric layer, where the nanoporous Al_2O_3 layer has a honeycomb-like composition. A microcavity of approximately 100-300 μm diameter is drilled through each foil, see Figure 1.3. The foils are aligned with concentric cavities, creating a single cavity between the two foils. Applying an AC waveform to the foils causes the configuration to act as a capacitor. The microcavity between the two foils concentrates the fringe electric field effects of the capacitor, resulting in an electric field of approximately 10^7 V/m. (Park, et al., 2002) A high pressure feed source supplies a propellant gas to the thruster, and as it enters the cavity the electric field initiates a Paschen-type breakdown of the gas into a plasma, which in turn increases the bulk temperature of the propellant. The specific mechanism by which the plasma is created and the propellant gas temperature is increased are discussed in Section 2.0. The high-temperature gas is then exhausted through a moderate Reynolds number nozzle producing thrust levels in the range of 1-5 mN.

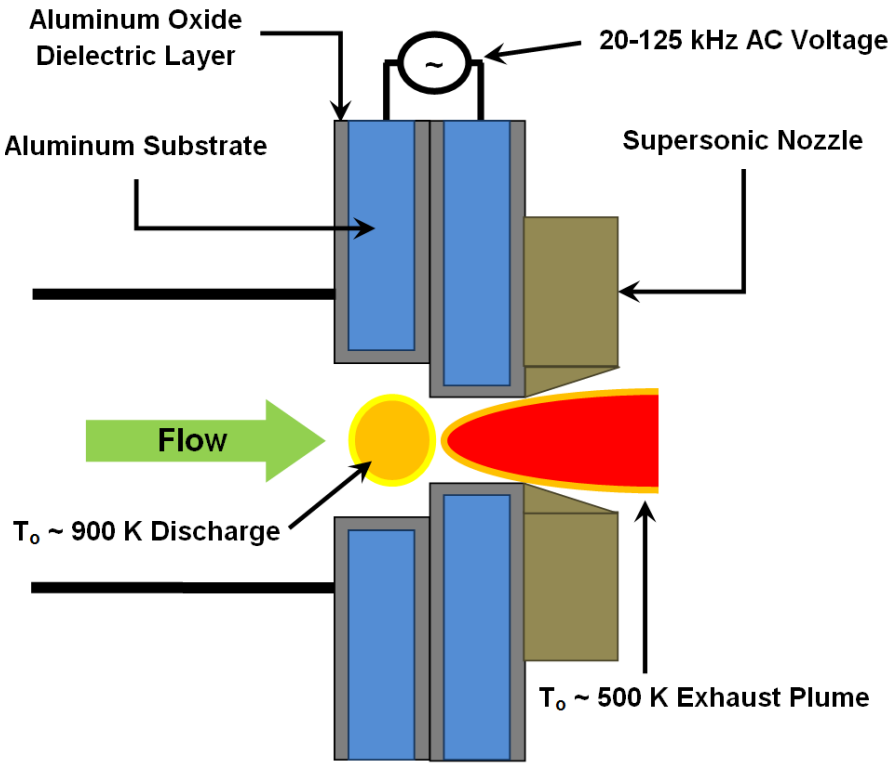

Figure 1.2: Schematic of the MCD thruster.

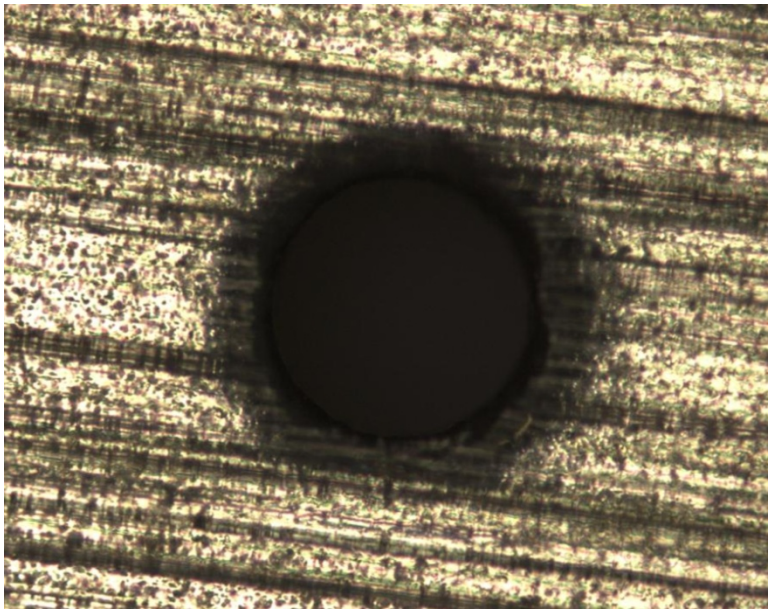

Figure 1.3: A 150 μm diameter, Al/Al_2O_3 system, microcavity.

Since the physical dimensions of the MCD thruster are extremely compact they are easily incorporated into nanosatellites. In addition, the high efficiency and low power of the MCD thruster means it does not require a large power supply or energy storage bank, and requires less propellant, reducing its overall system footprint. Finally, MCD devices have a positive V-I characteristic, see Figure 1.4. This allows for the parallel operation of multiple cavities in an array and enables the thrust level of an MCD thruster to be precisely tailored to mission requirements. In order to simplify fabrication, the majority of thrusters used during testing, the majority of thrusters used during testing are single cavity devices, although multiple cavity devices were used for several thrust measurements. Several studies of nanosatellite missions for which the MCD thruster would be uniquely suited have been developed, such as the station keeping, formation flying, and drag compensation maneuvers given in Ghosh. (Ghosh, 2009) Therefore, from a theoretical standpoint the MCD thruster is a viable option for nanosatellite propulsion and a sound basis for development is established.

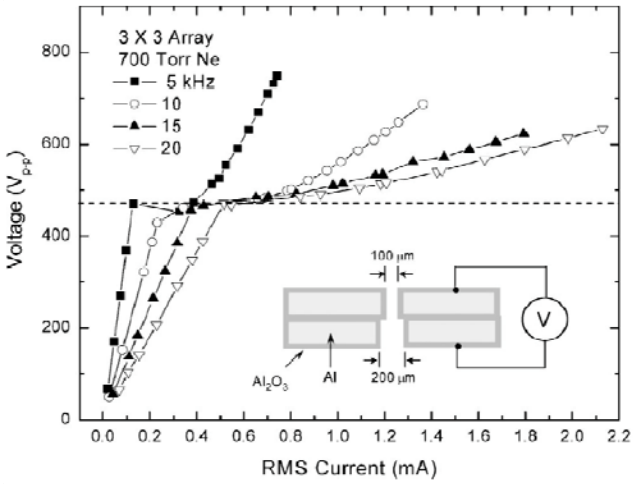

Figure 1.4: Positive V-I characteristic of a 3x3 array MCD device. Device geometry is shown on the inset.

1.2 Development Effort

Development of the MCD thruster is proceeding through two concurrent efforts: an experimental effort conducted at the Electric Propulsion and Optical Physics Laboratories at the University of Illinois, and a computational modeling effort at the University of Texas at Austin. This thesis will primarily focus on developments in the experimental effort, while a brief discussion regarding computational modeling can be found in Appendix B.

The experimental development of the MCD thruster centers around three types of testing: thrust measurements, Paschen breakdown minimum measurements, and thermal efficiency measurements. Thrust measurements of the MCD thruster are concerned with measuring the capabilities of the integral supersonic nozzle and validating its inclusion from an efficiency basis. Work by Bayt (Bayt, 1999) provides solid experimental data on of μm-scale supersonic nozzles for electrothermal thrusters as well as an exploration of their performance capabilities. There is little need to replicate his results and once the capabilities of the nozzles are verified, our treatment of them will be solely theoretical in nature. Overall this thesis deals primarily with the experimental measurements of the thermal efficiency of the MCD thruster as it is the largest factor with regards to thruster efficiency, although determination of the Paschen breakdown curve remains an important secondary objective.

1.2.1 Thermal Efficiency

As noted previously, the MCD thruster is an electrothermal type thruster in which the propellant gas is heated by a plasma breakdown and then ejected out a supersonic micronozzle. Since the MCD thruster is intended for use on power-limited nanosatellites, it must be highly efficient at converting stored electrical energy into increased thrust performance (the MCD thruster is capable of operating as an unpowered cold-gas thruster, so there will always be a base thrust level available to the satellite). While the overall thruster efficiency as described in equation (1.3) is dependent upon a number of parameters (Burton, 2009), the largest contributing factor to the total thruster efficiency is how effectively electrical energy is converted to thermal energy, denoted by the thermal efficiency:

$$\eta_{thermal} = \frac{\dot{m} C_p \Delta T_o}{P_{input}} \tag{1.6}$$

This equation demonstrates that for a fixed efficiency and mass flow rate the relationship between an increase in stagnation temperature and input power is linear. The relationship between increased temperature and increased thrust will be discussed in Section 2.2. The MCD thruster is an electrothermal thruster and so it is preferable to deposit as much heat into the propellant gas with as little applied power as possible. The primary consideration in maximizing the thermal efficiency is the ratio between the increase in the propellant gas temperature and the power required to achieve the increased temperature, note that the mechanism by which applied the waveform increases the propellant gas temperature will be discussed in Section 2.0. In general it is preferable to have the propellant gas heated to a significant degree in order to provide a thrust increase of between 1.5:1 to 3:1 over the unpowered cold gas case. There are however several issues associated with increasing the temperature of the propellant gas, with the most critical being wall heat losses. Additional factors include the reduced density and hence reduced Reynolds number that is a result of an increased ΔT.

The principal concern behind the ΔT factor is that increased propellant gas temperature leads to increased heat losses to the cavity walls. In fact, computational modeling suggests that wall heat loss is the single greatest energy sink in a microcavity discharge. In order to maximize the thermal efficiency of the MCD thruster, wall heat losses clearly must be minimized. An approximate calculation of the magnitude of wall heat losses and the key dependent parameters can be made with several basic assumptions. For the sake of simplicity a Reynolds number analogy will be used assuming an average value for the viscosity instead of a temperature dependent one. (Burton, et al., 2010) The localized wall losses are given by:

$$\dot{q}_w = \frac{\tau_w C_p (T - T_w)}{U} \tag{1.7}$$

Where τ_w is the local wall shear stress, related to the friction coefficient f and the fluid dynamic pressure $P_{dyn} = \rho\, U^2/2$ by $\tau_w = f g \frac{1}{2} \rho U^2$. For low Reynolds number (laminar) flows the friction coefficient is given by $f = 16/Re$ and the total wall heat loss can then be expressed as:

$$\dot{Q}_w = 4\pi\mu C_p (T_{o,max} - T_{o,c}) L \tag{1.8}$$

Since the mass flow rate $\dot{m}$ remains approximately constant during a test, it can be treated as a set parameter and has no further effect on the efficiency, while the wall length L is dependent on fabrication procedures and system footprint. The two variable parameters in the total heat loss equation are thus the specific heat c_p, which is dependent on the propellant gas mixture used and the ΔT_o parameter required to obtain a given level of thrust. The effects of the propellant gas mixture on performance are examined in section 7.3 while the effect of the ΔT_o parameter is explored in section 2.2.

2.0 THEORY OF OPERATION

2.1 Physics of Microcavity Discharges

The physics behind microcavity discharges originally stems from work performed on plasma display panels. (Park, et al., 2002) (Bitzer, 1966) (Slottow, 1976) The Laboratory for Optical Physics and Engineering at the University of Illinois has since developed a wide variety of devices based on MCD technology, primarily for use in various types of displays. The MCD thruster is an adaptation of existing MCD technology originally developed for plasma lighting, although several major changes were made to the technology for use in plasma thruster applications.

The process by which an MCD thruster operates is relatively straight forward and is similar in nature to the MCD process that occurs in other lower power devices, such as those used for illumination. In order to produce a thrust level greater than that of cold gas thrusters, an electrothermal thruster must heat the propellant gas, thereby increasing the energy of the flow which in turn increases the momentum of the propellant when expelled through a contoured nozzle. The mechanisms by which the MCD thruster adds energy to the flow will be explained in this section.

To understand the plasma formation and heating process that occurs in the MCD thruster, we begin with the basic structure of the MCD thruster: the electrode foils. Each foil consists of a pure aluminum substrate in which a cavity is drilled. An aluminum oxide dielectric layer is then grown on the surface of the aluminum substrate, including on the inner wall of the microcavity. Two (or more) foils are stacked on top of each other with the cavities in concentric alignment. The separation between metal substrates is equal to the thickness of each dielectric layer plus the thickness of any additional insulation material, such as a polyimide sheet. The sandwich of pure metal foil, aluminum oxide dielectric layer, insulation material if applicable, aluminum oxide dielectric layer, and pure metal foil comprises a capacitor where boundary effects are present both on the external edges and, critically, the internal microcavity.

Initiation of the plasma breakdown process begins when a propellant gas mixture is supplied to the thruster and an AC voltage of sufficient amplitude is applied to the electrodes. The propellant gas is driven through the microcavity by a pressure gradient, as the upstream pressure is normally 20-60 kPa while the downstream pressure is ~0 kPa. The flow reaches Mach 1 at the cavity exit, which is designed to have the minimum flow area. This converging design ensures the heating will take place in the subsonic region of the flow. The AC voltage is applied to the foils at 25-150 kHz, with the upstream electrode ‘hot,’ and the downstream electrode grounded. Since the electrodes are in a capacitive configuration, as the voltage waveform rises the strength of the electric field between the two foils increases. The electric field fringe effects present at the capacitor boundary are concentrated in the small diameter of the microcavity. This leads to a much higher electric field inside the cavity, on the order of 10^7 V/m, than between the flat surfaces of the foils. As the voltage continues to rise and the electric field in the cavity continues to increase, ionized particles naturally present in the propellant gas gain energy, acting as a seed for a breakdown. These natural ions and electrons are accelerated by the electric field gaining velocity until they collide with

unexcited atoms. The impact with an unexcited particle has a several possible outcomes, depending on a variety of factors including the particle mobility, the density of the propellant gas, and the collision parameters including its elastic or inelastic nature and the cross section of the particles involved. There are three possible outcomes that lead to increased bulk energy term and hence increased propellant gas temperature. The first case is that as a result of the collision the unionized particle simply gains momentum from the impact, but is neither excited nor ionized. In the second case the unexcited particle gains enough energy to become excited but remains unionized, although particles in the excited state are a significant contribution to the energy of the gas. In the third case the impact imparts enough energy to the unionized particle to cause it to become ionized, releasing an electron in the process. According to computational modeling performed by Sitaraman and Raja (Sitaraman, 2010) these ionized particles are the largest contributors of energy to the flow.

The multiple impacts create a wave of excited particles resulting in the creation of an ionized (ionization fraction ~10^{-5} with respect to neutral) gas, or plasma. Since the excited and ionized particles have a higher energy than the surrounding unionized particles, collisions with these neutral particles increases the energy level of the bulk gas, which is manifested on a macro scale as an increase in temperature. The increased flow temperature leads to a greater sonic velocity and depending on the flow configuration either a reduction in density and mass flow rate or an increase in pressure (and hence an increase in thrust). On a flight thruster an appropriately contoured supersonic nozzle would be added downstream of the throat increasing the velocity of the propellant exhaust beyond Mach 1, providing an additional boost to the thrust and I_{sp}.

2.2 Thrust Equations

Although propellant heating in the MCD thruster occurs through a different process than in a traditional jet or rocket engine, the equations that govern the flow of the heated propellant are the same. The flow inside the MCD thruster can be approximated as Rayleigh heating followed by isentropic acceleration through a converging nozzle, and finally acceleration through a supersonic diverging nozzle. Since the primary test configuration of the MCD thruster does not include a supersonic nozzle, the following discussion will be limited to the subsonic regime only. Discussion of supersonic nozzle parameters can be found in section 2.2.2.

As is the case with virtually all thermal-fluid aerospace propulsion systems, flow inside the MCD thruster is driven by a pressure gradient. At the nozzle throat, located at the exit plane in test configuration, the flow reaches the sonic condition. Therefore the thrust equation can be expressed as a function of the flow conditions at the throat:

$$F = C_F p_o^* A^* \tag{2.1}$$

Although equation (2.1) is the primary form of the thrust equation, thrust can also be expressed as:

$$F = \dot{m} U_e \tag{2.2}$$

Equation (2.2) defines the relationship between thrust and the propellant mass flow rate. The mass flow rate can further be expressed as a function of the flow conditions at the throat:

$$\dot{m} = \rho^* U^* A^* \tag{2.3}$$

Finally, in order to express the mass flow in terms of the other measureable parameters the addition of common isentropic flow relations result in the following expression for mass flow in terms of the Mach number:

$$\dot{m} = A^* \frac{p_o}{\sqrt{T_o}} \sqrt{\frac{\gamma}{R}\left(\frac{2}{\gamma+1}\right)^{(\gamma+1)/(\gamma-1)}} \tag{2.4}$$

Equation (2.4) is a critical governing equation for the flow conditions that occur inside an MCD thruster during discharge, as the parameter $p_o/\sqrt{T_o}$ can be directly related to the stagnation temperature and pressure ratios as determined by the Rayleigh equations.

2.2.1 Rayleigh Equations

Since the MCD thruster operates as an electrothermal device, the dominant regime is Rayleigh flow, or flow with heat additions. Since equation (2.1) is ultimately dependent on the throat pressure, a relationship between the increase in temperature and the corresponding increase in thrust must be developed. The relevant forms of the necessary equations can be derived from the energy equation (Anderson, 2004):

$$C_p T_1 + \tfrac{1}{2}U_1^2 + q = C_p T_{o1} + q = C_p T_2 + \tfrac{1}{2}U_2^2 = C_p T_{o2} \tag{2.5}$$

For $q = 0$ (adiabatic) we can rewrite the energy equation as:

$$\frac{T_o}{T} = 1 + \frac{\gamma-1}{2}M^2 \tag{2.6}$$

and

$$\frac{p_o}{p} = \left(1 + \frac{\gamma-1}{2}M^2\right)^{\gamma/(\gamma-1)} \tag{2.7}$$

and

$$\frac{\rho_o}{\rho} = \left(1 + \frac{\gamma-1}{2}M^2\right)^{1/(\gamma-1)} \tag{2.8}$$

Then, from equation (2.5):

$$q = C_p(T_{o2} - T_{o1}) \tag{2.9}$$

We can rewrite in terms of the Mach number:

$$\frac{p_2}{p_1} = \frac{1+\gamma M_1^2}{1+\gamma M_2^2} \tag{2.10}$$

Additionally, a similar relation can be written for the temperature ratio using equations (2.6) and (2.10):

$$\frac{T_2}{T_1} = \left(\frac{1+\gamma M_1^2}{1+\gamma M_2^2}\right)^2 \left(\frac{M_2}{M_1}\right)^2 \tag{2.11}$$

Combining equations (2.7) and (2.10) we obtain:

$$\frac{p_{o2}}{p_{o1}} = \frac{1+\gamma M_1^2}{1+\gamma M_2^2}\left(\frac{1+\frac{\gamma-1}{2}M_2^2}{1+\frac{\gamma-1}{2}M_1^2}\right)^{\gamma/(\gamma-1)} \tag{2.12}$$

Combining equations (2.6) and (2.12) we obtain:

$$\frac{T_{o2}}{T_{o1}} = \left(\frac{1+\gamma M_1^2}{1+\gamma M_2^2}\right)^2 \left(\frac{M_2}{M_1}\right)^2 \left(\frac{1+\frac{\gamma-1}{2}M_2^2}{1+\frac{\gamma-1}{2}M_1^2}\right) \tag{2.13}$$

Equations (2.12) and (2.13) can then be used to calculate the magnitude of the temperature rise and pressure loss that occurs in the Rayleigh flow region. Determination of the pressure loss ensures that the proper temperature is used to calculate the thermal efficiency. Calculation of the magnitudes of equations (2.12) and (2.13) is a two-step process. First, since the diameter of each microcavity is known, the area ratio of the converging nozzle can be calculated. Since the flow reaches sonic velocity at the throat due to the large pressure gradient in the, the area-Mach number relation can be used to calculate the upstream Mach number required for the sonic condition:

$$\left(\frac{A}{A^*}\right)^2 = \frac{1}{M^2}\left[\frac{2}{\gamma+1}\left(1+\frac{\gamma-1}{2}M^2\right)\right]^{(\gamma+1)/(\gamma-1)} \tag{2.14}$$

The Mach number derived from equation (2.14) becomes the parameter M_2 in equations (2.12) and (2.13). With the addition of equations (2.2) and (2.4) the degree of heating and the resulting increase in thrust can be calculated and the baseline performance of the thruster measured. One additional factor is the calculation of the nozzle efficiency and thrust coefficient of the integral supersonic micronozzle.

2.2.2 Micronozzle Performance

A second factor of importance in determining the overall thruster efficiency is the nozzle efficiency, given by:

$$\eta_{nozzle} = \frac{F_{actual}}{F_{ideal}} \tag{2.15}$$

Bayt (Bayt, 1999) discovered that the key parameter in determining the efficiency of a micronozzle is the throat Reynolds number since it is a first order factor in both the viscous losses and wall heat losses of the nozzle. Ultimately Bayt determines that in order for a μm-scale supersonic nozzle to be effective, a thrust coefficient of > 1.2 must be obtained; a thrust coefficient lower than this incurs unacceptable viscous losses and a simple near-isentropic subsonic nozzle is preferable. Although there are a number of factors that determine the thrust coefficient, in general for μm-scale nozzles if the throat Reynolds number exceeds 1000 then the addition of a supersonic nozzle is worthwhile from an efficiency standpoint.

By making several basic assumptions with regards to the parameters of an operational MCD thruster it is possible to estimate the required minimum feed pressure for an integral supersonic micronozzle. The Reynolds number is defined as:

$$Re \equiv \frac{\rho U d}{\mu} \tag{2.16}$$

For an argon propellant system, an approximate value for the degree of heating desired in an MCD thruster is 900 K. A throat diameter of 300 μm may also be assumed. From these parameters it is easy enough to calculate that the required feed pressure is approximately 100 kPa. Given that this pressure is well within the capabilities of even nanosatellite propellant tanks, it is clear that the inclusion of a supersonic nozzle is a viable option for the MCD thruster.

3.0 TECHNICAL APPROACH

3.1 Experimental Setup

3.1.1 Overview

As discussed in section 1.2, the primary performance parameter being investigated is the thermals efficiency. The thermal efficiency test results given in this document are obtained from a single test configuration, but the MCD thruster has been run in two different configurations: the first to measure micronozzle performance and the second to measure the Paschen breakdown minimum and thermal efficiency. The two general test configurations used for performance measurements directly correspond to the vacuum tank in which the testing is performed. During the initial stages of testing the MCD thruster was placed on a compact thrust stand inside a 1.2 m^3 capacity vacuum tank in order to determine the nozzle efficiency of the device. For the thermal efficiency testing phase the thruster was moved to a smaller 0.15 m^3 capacity vacuum tank to alleviate external plasma glow phenomenon.

3.1.2 Test Facilities and Equipment

3.1.2.1 Vacuum Tanks

Experimental testing of the MCD thruster was undertaken in the Electric Propulsion Laboratory (EP Lab) at the University of Illinois. The EP Lab is equipped with two vacuum tanks: a large 1.2 m^3 tank in which a Watt's pendulum-type thrust stand is installed, see Figure 3.1, and a smaller 0.15 m^3 vacuum tank which has a transparent front face for observing test runs, see Figure 3.2.

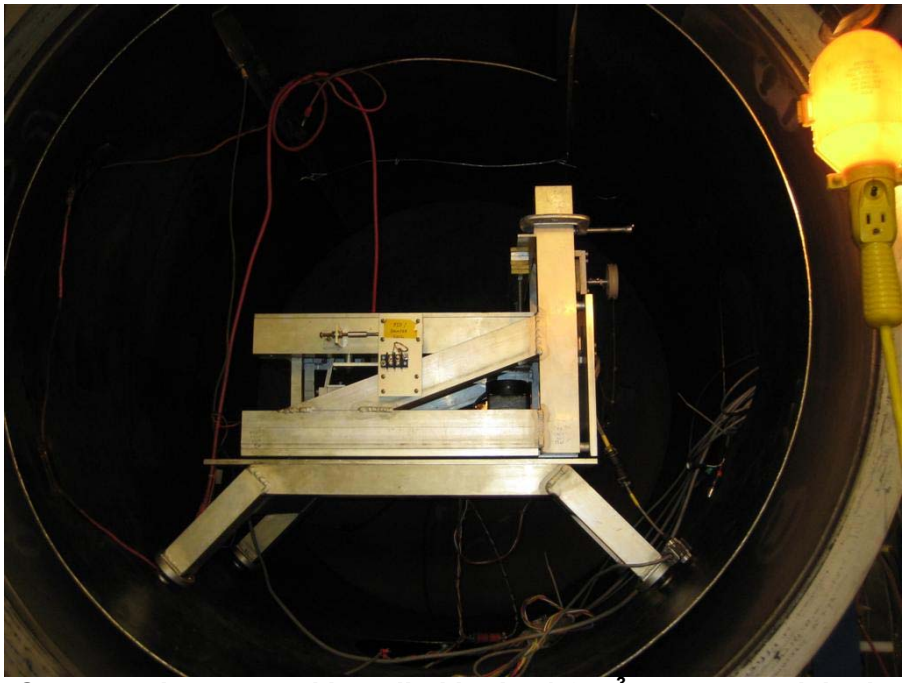

Figure 3.1: Compact thrust stand installed in the 1.2 m^3 vacuum tank in the EP Lab at UIUC

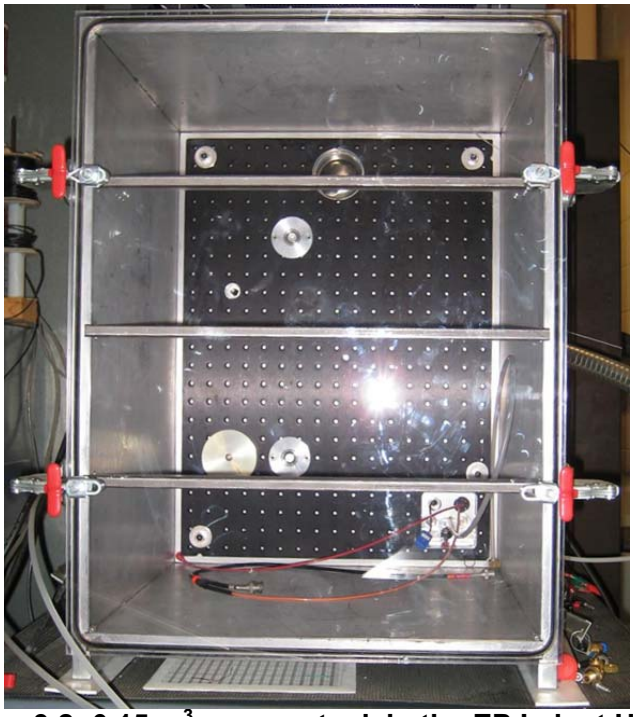

Figure 3.2: 0.15 m^3 vacuum tank in the EP Lab at UIUC.

Use of the 1.2 m^3 vacuum tank has a number of advantages and disadvantages with regards to testing, the most notable of which is that the compact thrust stand (described in Wilson and Burton (Wilson, et al., 1997)) was built specifically to fit snugly inside the tank, restricting thrust measurements to the large tank only. The 1.2 m^3 tank utilizes a three stage pump-down system to achieve vacuum; the first stage is comprised of a mechanical displacement pump which can achieve a minimum pressure of approximately 5 Torr after approximately 2 hours. The second stage consists of two sequential roots-type pumps which can achieve a minimum background pressure of approximately 100 mTorr, which requires approximately 1.5 hours. The third stage consists of an axial nanomolecular turbopump, capable of achieving minimum background pressures of 10^{-5} Torr after approximately 2 hours. The internal capacity of the 1.2 m^3 vacuum tank is divided into two sections: a larger barrel section which houses the thrust stand and the wiring for the MCD experiments, and a smaller cross-junction section which houses a gallium electromagnetic thruster. Although the two sections on the tank share a common depressurized volume, an internal baffle prevents direct contact between them.

The 0.15 m^3 vacuum tank was originally built to test the deployment of a solar sail material between two Cube Sat 10 cm units and is sized appropriately. The 0.15 m^3 vacuum tank utilizes a two stage pump down system. The first stage consists of a mechanical displacement pump which is capable of achieving a minimum background pressure of approximately 1.5 Torr in 45 minutes. The second stage consists of an axial nanomolecular turbopump, capable of achieving pressures of approximately 10 mTorr after an additional 45 minutes. In the initial stage of testing the entire thruster was placed inside the tank, but glowing on the external surfaces of the electrode foils

hampered power measurements. The thruster was then moved to the outside of the tank, with only the microcavity exposed to the vacuum (see Figure 3.10), solving the glowing problem.

3.1.2.2 Power Supply

The voltage waveform is supplied to the MCD thruster through a 3-stage process. The initial signal is generated by a Victor VC2002 function generator. A Mackie FR800 800 W 2-channel amplifier was originally used to boost the signal to higher voltage levels, in later tests it was replaced by a QSC RMX 1450 1400 W two-channel amplifier. In the final stage the voltage of the waveform is further boosted by a 1:100 turn ratio custom built solid core transformer. The power supply is shown in Figure 3.3, and a connection diagram is shown in Figure 3.4.

Figure 3.3: MCD Thruster power supply. Top left: Victor VC2002 Function Generator. Top Right: Custom 100:1 Solid Core Transformer. Center: QSC Audio RMX 1450 1400 W 2 Channel Amplifier. Center Low: Mackie FR800 800 W 2 Channel Amplifier

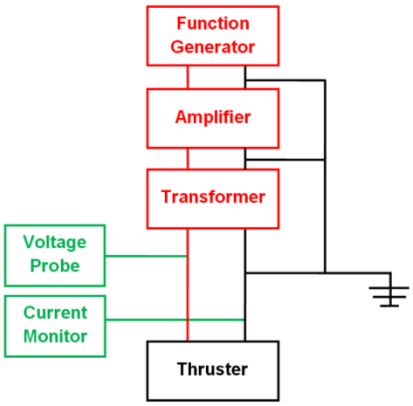

Figure 3.4: Connection diagram for the MCD thruster power supply and instrumentation.

3.1.2.3 Instrumentation

The same instrumentation is used in both MCD thruster test configurations: mass flow and pressure measurements are made by two mass flow sensors and a pressure transducer while power measurements are made by a voltage probe and a current monitor connected to an oscilloscope. The thrust stand is also used for thrust measurements. In order to facilitate data collection, a computer running National Instruments LabVIEW and Mathworks MATLAB is used to record all measureable parameters during testing. The LabVIEW interface can display the real time values of all connected instrumentation and record it for later analysis while MATLAB is used to record 'snapshot' measurements. The majority of the instrumentation is connected to the computer by means of a National Instruments data acquisition card, although the oscilloscope is connected through the standard local-area network. A National Instruments SCXI-1000 Data Acquisition Box serves as an interconnect between the data acquisition card and the instrumentation, see Figure 3.5.

Figure 3.5: National Instruments SCXI-1000 Data Acquisition Box

Figure 3.6: Flow sensors. Top Left: Omega Engineering FMA3104 series MFM. Top Right: Omega Engineering FMA3107 series MFM. Center Bottom: Cole-Parmer 68072-52 Type Pressure Transducer.

The mass flow rates of the propellant gases are measured using two Omega Engineering mass flow sensors: a FMA3107 sensor with a flow rate of 0-2000 standard cubic centimeters per minute (SCCM) calibrated for helium, and a FMA3104 sensor with a flow rate of 0-200 SCCM calibrated for air, Figure 3.6. The mass flow sensors are connected to the LabVIEW interface through the SCXI-1000 Data Acquisition Box. There are two important notes with respect to the mass flow sensors. The first is that the mass flow sensors have needle valves which induce a sonic throat condition (two of four such points in the propellant feed system, the other two are at the metering valves) and since the pressure supplied from the gas bottles remains constant, then once the downstream pressure has been set by the position of a metering valve the mass flow through the flow meters remains constant. A second note is that although every effort has been taken to ensure the integrity of the propellant feed system, the propellant gasses are supplied at below-atmospheric pressure and it is likely that some small

amount of laboratory air seeps into the propellant flow and is not detected by the mass flow sensors.

Line pressure measurements are conducted with a Cole-Parmer 68072-52 type piezoelectric pressure transducer. The transducer has an effective range of 0-50 psia (0-345 kPa), with a resolution of 0.1 kPa, see Figure 3.6. The transducer is also connected to the SCXI-1000 Data Acquisition Box and in turn to LabVIEW. Measurements made by the pressure transducer are displayed in real time on the LabVIEW interface and are also used to determine the extent of the pressure rise observed during operation of the thruster.

Voltage and current measurements are performed by a Tektronix P5100 100x voltage probe and a Pearson Electronics 1:1 V/A current monitor connected to a Tektronix TDS3034B oscilloscope, see Figure 3.7. The voltage and current measurements are taken at the points shown in Figure 3.4. The voltage and current measurements can be displayed in real time and recorded by LabVIEW, or a 'snapshot' of the waveforms can be made using MATLAB. During testing it was discovered that although LabVIEW has the advantage of displaying real time values, it is unable to resolve the waveform to a sufficient degree of accuracy to perform measurements, and thus power measurements are taken with MATLAB.

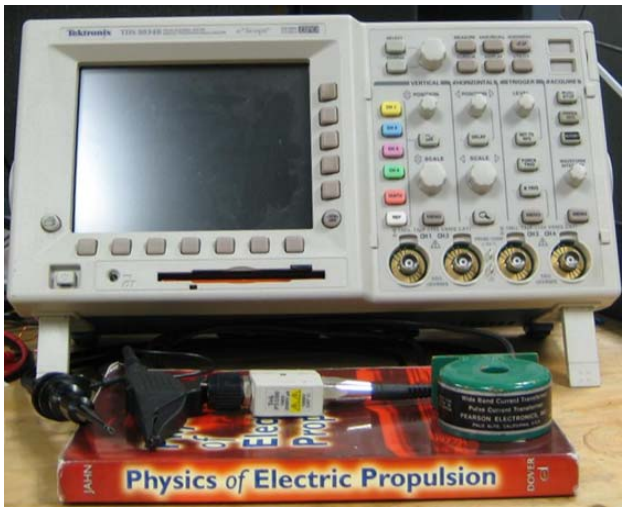

Figure 3.7: Power Measurement Instrumentation. Top: Tektronix TDS 3034B. Bottom Left: Tektronix P5100 Voltage Probe. Bottom Right: Pearson Electronics 1:1 Current Monitor.

3.2 Experimental Procedure

3.2.1 Thrust Measurements

In order to validate the performance of the integral supersonic nozzle thrust measurements are taken using a compact thrust stand. The thrust stand functions as an inverted pendulum where the deflection of the main platform is measured by a linear variable differential transformer (LVDT). The deflection of the thrust stand during thruster operation is compared to the deflection produced by a set of calibration weights to obtain a thrust measurement. The procedure for performing a thrust measurement is described below.

During the initial stage of a test run, a set of five calibration weights with known mass (34.5 mg) are sequentially applied to the main platform by means of small pulley fixed to the stand frame. During this process the deflection of the main platform is measured in the form of increased voltage from the LVDT and recorded by LabVIEW. An exemplary plot of the deflection can be seen in Figure 3.8. Since each calibration weight is of

known mass, and the monofilament that connects them is of negligibly small mass the step in the deflection that occurs as each weight comes to bear on the platform can thus be equated to a known force. Each weight is applied in sequence, and then the process is reversed producing the two-way stepped plot seen in Figure 3.8.

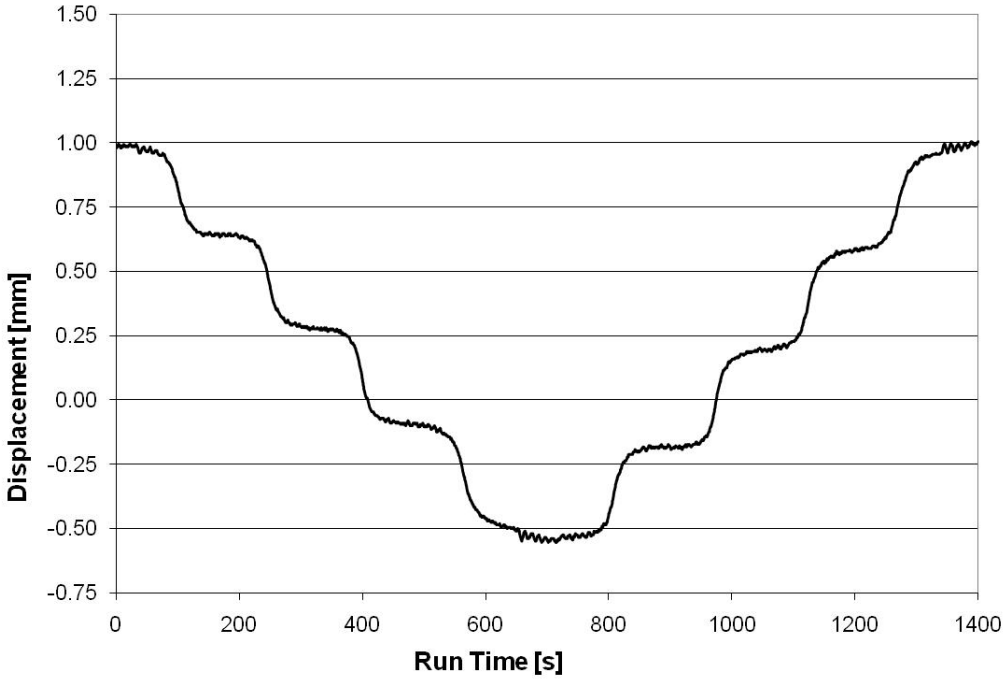

Figure 3.8: A typical calibration curve for the compact thrust stand at UIUC. Each step corresponds to a force of approximately 0.338 mN.

Once the calibration plot has been produced, it is a simple matter to find a slope and thus a linear calibration fit. After the calibration fit has been obtained, flow of the propellant gas to the thruster is initiated, with adjustments to flow rates made as necessary in order to achieve the desired pressure and propellant gas mixture. An initial discharge coefficient is obtained in order to determine both the degree of concentricity of the cavity alignment and to serve as a baseline for later cavity damage comparisons. The discharge coefficient is an experimentally determined parameter defined as:

$$C_d \equiv \frac{\dot{m}_{actual}}{\dot{m}_{ideal}} \tag{3.1}$$

As defined in equation (3.1), the discharge coefficient functions as a correction factor for various losses encountered in fluid flow through an area reduction or orifice. (Cengel, 2004) In the ideal case the mass flow rate would simply be a function of the cross-sectional area, the flow velocity, and the fluid density. Due to viscous and friction effects the actual mass flow is always less than the ideal case, and thus C_d is always less than 1.

The discharge coefficient is calculated numerically from a comparison between the actual throat temperature and the ideal throat temperature. Initially, the throat pressure is calculated by:

$$p^* = p_o \left(\frac{2}{\gamma + 1}\right)^{\gamma/(\gamma-1)} \tag{3.2}$$

where γ is the calculated specific heat ratio for the mixture as a whole. The measured throat stagnation temperature is then calculated by:

$$T_o^* = \frac{\gamma}{R_s \left(\frac{\dot{m}}{p^* A^*}\right)^2} \tag{3.3}$$

where the effective throat area is calculated by $A^* = C_d A$. Since all parameters other than C_d are fixed, the measured throat stagnation temperature is then compared to the ideal throat stagnation temperature, given by:

$$T_{o,ideal}^* = T_o \frac{2}{\gamma + 1} \tag{3.4}$$

By setting $T_o^* = T_{o,ideal}^*$ it is possible to solve for the discharge coefficient. For a properly aligned and undamaged thruster typical C_d values are in the range of 0.85-0.98.

After the discharge coefficient is established and the desired flow parameters are reached, the propellant flow is temporarily shut off, although the metering valves retain their previous positions. Once the thrust stand has settled back to the neutral position, the flow is initiated again, with the same line pressure and propellant gas composition as before. The deflection of the thrust stand between the neutral and the cold flow states gives the cold thrust value, which indicates the base performance level of the MCD thruster. An example of typical cold thrust results can be seen in Figure 3.9.

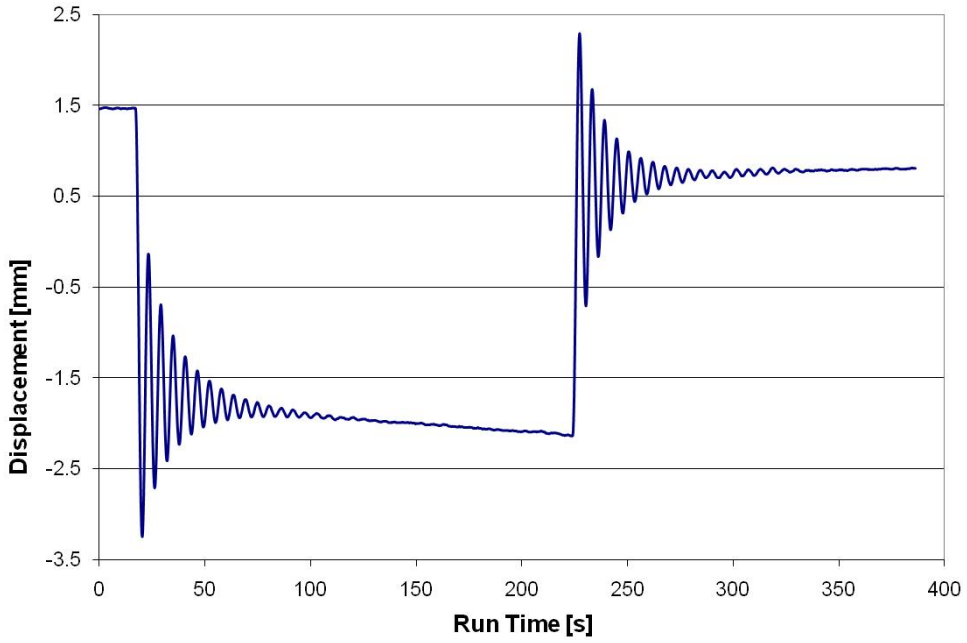

Figure 3.9: A typical cold thrust displacement plot. The 'ringing' sections are due to the long-period oscillations resulting from the displacement overshooting the equilibrium point. This plot is from a 4-cavity, 120 μm throat diameter, supersonic nozzle electrode running pure neon at 240 kPa. The average thrust value is 2.7 mN. Due to thruster orientation, positive thrust corresponds to negative displacement.

In addition to the cold thrust level, the baseline thrust measurement also makes it possible to calculate the thrust coefficient, C_f, for a supersonic nozzle. The thrust coefficient is defined as:

$$C_f \equiv \frac{F}{p^* A^*} \tag{3.5}$$

Following the determination of the baseline cold thrust value and the thrust coefficient, power is supplied to the thruster and a discharge is initiated. An increase in the displacement of the thrust stand and the line pressure are both indications of an increased thrust level, since the thrust is given by equation (2.1). Additionally, depending on configuration, the thrust may remain constant while the mass flow rate drops, indicating an increased I_{sp}. The increase in thrust stand displacement or decrease in $\dot{m}$ in contrast to the cold case is measured and the hot thrust value determined. From these measurements it is possible to determine the thrust coefficient using equations (2.1) and (3.5).

3.2.2 Paschen Breakdown Minimum Measurements

The second type of measurements made during testing of the MCD thruster are related to the determination of the minimum voltage required to initiate a breakdown of the propellant gas for any given flow conditions. Since the plasma formation inside the microcavity is initiated by an electric field, MCD devices follow the general principles of a Paschen-type breakdown. (Cobine, 1958) Briefly, this means that once the electric field inside the microcavity that results from the capacitor fringe effects reaches a certain limit the propellant gas breaks down into plasma. The parameters that determine the point at which breakdown occurs are the pressure of the gas, the electrode separation distance, and the voltage applied to the two plates of the electrode. For the purposes of gaseous electronics such as the MCD thruster it is convenient to denote the product of the electrode separation distance and the gas pressure as the parameter pd. (Cobine, 1958)

A concern with many micrometer scale electronic devices is the voltage levels that are required for operation, and the MCD thruster is no exception. Since the aluminum oxide layer has a nominal thickness of only 10-20 μm, any cracks or other flaws can lead to arcing between the electrode foils and the rapid destruction of the thruster. In addition, higher voltage levels carry various system penalties such as requiring more robust transformers and increased insulation; therefore it is beneficial to accurately determine the minimum voltage necessary for optimal thruster operation. The most important task in this regard is the determination of the voltage required to initiate breakdown of the propellant gas, known as the Paschen breakdown minimum. Testing for the Paschen breakdown minimum serves several purposes: it allows for the creation of a Paschen curve which can be used to predict the voltage required for breakdown at numerous pd values; it gives a good estimate of the voltage range required for optimal thruster operation; and it gives insights into the basic physics of the MCD process. In regards to the last purpose, one key purpose of Paschen breakdown testing is to determine the correct value to use for the electrode separation distance. Earlier work by Park et al. (Park, et al., 2002) suggested that in static (no flow) devices the cavity diameter was the

dominant d term in the pd characteristic. Subsequent testing of the MCD thruster revealed that in a flowing system the distance between pure metal substrates is the dominant d term.

The process by which the Paschen breakdown minimum of the MCD thruster is determined for a given pd value is straightforward. Testing is performed in the 0.15 m^3 vacuum tank. The thruster is mounted so that only the microcavity and the discharge shroud are exposed to the vacuum while the rest of the thruster is in lab air, see Figure 3.10 for details. Propellant flow to the thruster is initiated, and the desired flow conditions are achieved. Power is applied to the electrode and the voltage is gradually increased. Once the voltage reaches the Paschen minimum, a sharp peak appears in the current waveform indicating a breakdown. Two features of the breakdown are important to note: first, the peak forms near instantaneously over the course of a single cycle so the moment of breakdown can be determined with a high degree of accuracy; second, the voltage tends to shift slightly after a breakdown and both the instantaneous and settled voltage values are recorded. The discharge is then shut off, the flow conditions are adjusted as necessary, and the test is repeated. Once sufficient data points have been gathered, the resulting curve can be generalized over a range of pd values. The results of the MCD thruster Paschen testing are given in Section 7.2.

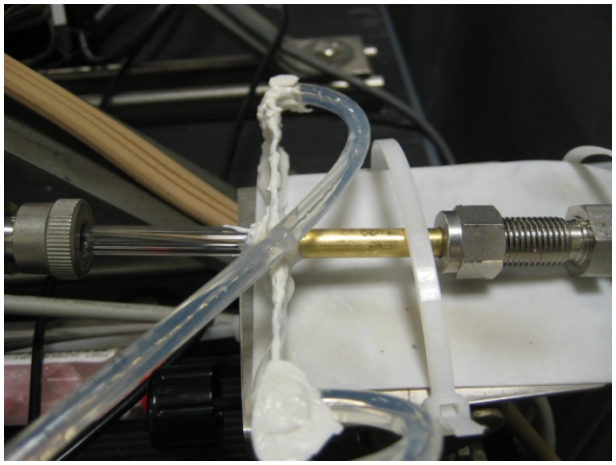

Figure 3.10: Thruster-vacuum tank interface. The propellant is fed through the brass tube on the right, while the heated propellant exhaust through the glass tube on the left. The glass tube is secured to the vacuum tank with an Ultra-Torr fitting.

3.2.3 Heating and Thermal Efficiency Measurements

During the initial phase of development the principle type of testing undertaken to validate the performance of the MCD thruster is the determination of the thermal efficiency through heating and power measurements. The thermal efficiency of the MCD thruster is defined in equation (1.6) and repeated for the sake of convenience:

$$\eta_{thermal} \equiv \frac{\dot{m} C_p \Delta T_o}{P_{input}} \tag{3.6}$$

Since both the mass flow rate and the specific heat of propellant gas mixture are set by the initial flow conditions, the two variable parameters remaining are the input power P_{input} and the change in temperature ΔT_o over the cold thrust case. In order to perform a thermal efficiency test the desired flow conditions are first set and an initial discharge coefficient is taken. Voltage is then applied to the electrode and the initial and settled voltages are recorded to establish a Paschen minimum curve. The voltage is then increased until a visible stable discharge with a bright core and a pronounced exhaust plume is observed or when voltage amplitude reaches a value 1.2 kV peak-peak, as

higher values are harmful to the electrodes. Once one of these conditions is met, the amplitude of the voltage is held steady, indicating an approximately constant level of power is being supplied to the thruster. Since the mass flow rate is constant, the increased temperature of the propellant gas results in an increase in the stagnation pressure, as measured by the pressure transducer. During this period of maximum heating multiple voltage and current waveform measurements are made to calculate the input power level.

The input voltage and current waveforms are measured by the voltage probe, current monitor, and oscilloscope seen in Figure 3.7, connected at the points indicated in Figure 3.4. The oscilloscope is connected to MATLAB which enables precise determination of the input power. The most desirable power measurement is the mean cycle power of the waveform, as this gives the best estimate of the power required by the thruster. Due to variations in the frequency, amplitude, and peak location precise automated power measurements are difficult to make, especially with regards to the mean cycle power. Additionally, during optimal heating a number of high-frequency pulses occur in the current and voltage waveforms, as seen in Figure 3.11. These pulses have a frequency of approximately 1 MHz, the pulse width is approximately 250-500 ns, and the amplitude of the pulses is approximately equal to the sinusoidal amplitude of the base waveform. Accordingly, the final process for power measurement involves the manual determination of the period of the waveform as earlier efforts at using Fourier analysis to determine the period were unsuccessful. Determination of the mean cycle power is made through the following steps:

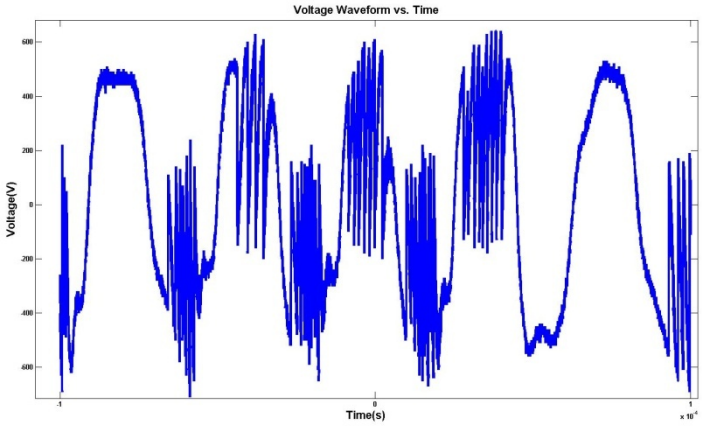

Figure 3.11: Typical voltage waveform during optimal heating. The applied frequency of 25 kHz shifts during discharge by up to 5 kHz from the nominal value. Note that high-frequency pulses did not occur in 3 of the half cycles.

- Once the initial discharge has been achieved the voltage supplied to the electrode is increased to the desired value. Over the course of the test run the supplied voltage is kept steady resulting in an approximately constant power level. A power measurement is also made at the initial breakdown point.
- During a test run a MATLAB subroutine is used to record a 'snapshot' of the waveform. The oscilloscope is capable of recording 10,000 data points per sample, with two channels in use both the voltage and current samples are composed of 5,000 data points.
- The MATLAB function takes three separate samples of the waveform, at 10 second intervals.
- Four separate measurements are taken resulting in a total of 12 samples.

- The waveforms collected in each sample are plotted and the data cursor function in MATLAB is used to manually pick out an integral number of cycles over which the mean cycle power calculation will be performed.
- For each sample the instantaneous current and voltage values are multiplied, summed over the cycle or cycles, and then multiplied by the cycle period, resulting in the mean cycle power. Typical deviation of input power between sample measurements is less than 15% for 12 samples.
- The 12 samples are averaged to obtain the mean cycle power for the run.

Once the necessary power measurements have been made, the line pressure is allowed to settle to a steady state value so that a maximum ΔT_o value may be obtained. The applied power is then shut off and the flow is allowed to settle so that a final discharge coefficient can be taken in order to detect any damage to the microcavity.

There are two possible ways to determine the heating that occurs during the discharge. The first is a simple isentropic pressure ratio calculation, which yields the heating in the ideal case. Since the initial temperature and the initial and peak pressures are known, and for an isentropic flow the change in temperature changes with the square of the change in pressure, the peak discharge temperature can be calculated by:

$$T_{o,disch} = \left(\frac{p_{disch}}{p_{init}}\right)^2 T_{o,init} \tag{3.7}$$

Equation (3.7) holds when $M_2 << 1$, i.e. when there is a large convergence area ratio, although the MCD thruster is more accurately modeled as flow through a heated duct (Rayleigh flow) followed by flow into a converging nozzle. As a result, knowledge of the peak initial stagnation pressure, the initial stagnation temperature, and the mass flow rate allows for calculation of the heated stagnation temperature. For a converging nozzle, the incoming Mach number required to drive a constant mass flow can be determined from equation (2.14). The Mach number extracted from equation (2.14) becomes M_2 in equations (2.12) and (2.13). Then the final necessary equation is the choked mass flow equation, given in equation (2.4). Since the converging nozzle portion of the MCD thruster is assumed to be isentropic, the values p_{o2} and T_{o2} which result from the Rayleigh heating may also be used in the above mass flow equation. Therefore using equations (2.4), (2.12) , and (2.13) both the degree of heating and the corresponding stagnation pressure loss resulting from the Rayleigh flow section can be calculated. Once the peak discharge temperature has been calculated the thermal efficiency is determined using equation (1.6). Heating and thermal efficiency results are given in section 7.3.

4.0 COMPUTATIONAL MODEL

4.1 Plasma Dynamics Model

A self-consistent multi-species multi-temperature continuum model is used to describe the discharge phenomenon in the MCD thruster. The plasma governing equations are solved over an unstructured mesh using a semi-implicit finite volume method. The model also uses finite rate argon chemistry (Deconinck, 2009) which will be described below. The electrons are assumed to have a different temperature compared to the heavy species. The heavy species (ions, metastables and neutrals) are assumed to have a common gas temperature which is a reasonable assumption due to small energy transfer mean free paths (Deconinck, 2008). The continuum method described here is reasonably valid (Deconinck, 2008) at the current operating pressures (1-40 kPa) and characteristic dimensions (on the order of 100 μm).

4.1.1 Plasma Governing Equations:

The species continuity equation is solved to obtain the number densities of ions, metastables and electrons. It is given by:

$$\frac{\partial n_k}{\partial t} + \vec{\nabla}.\vec{\Gamma}_k + \vec{\nabla}.\left(n_k \vec{V}\right) = \dot{G}_k \tag{4.1}$$

k = 1…K_G (k is all species except a single dominant background species)

Here n_k is the number density of species k, $\dot{G}_k$ is the species production rate of species k due to reactions and $\vec{\Gamma}_k$ is the particle flux given by the drift-diffusion approximation shown in equation (4.2). $\vec{V}$ represents the bulk fluid velocity,

$$\vec{\Gamma}_k = -\mu_k n_k \vec{\nabla}\varphi - D_k \vec{\nabla} n_k \tag{4.2}$$

Here, μ_k is the species mobility, φ the potential and D_k is the diffusion coefficient. The drift-diffusion approximation is reasonably valid for plasmas in millimeter and larger length scales. For microplasmas such as in the current study the ion momentum equation is solved to obtain the ion flux used in the continuity equation. It has been seen that the ion momentum equation will yield solutions at least 20% off from the solutions obtained using the drift-diffusion approximation (Deconinck, 2008). In the current model, the drift-diffusion approximation is applied only to the electrons and the metastable species. The density of the background neutral species is updated using the ideal gas law.

The electron energy equation is solved to obtain the electron temperature T_e, necessary for the production term calculation in the continuity equation for electron impact reactions. It is also used to find the transport coefficients associated with the electrons. It is given by

$$\frac{\partial e_e}{\partial t} + \vec{\nabla}.\left[(p_e + e_e)\left(\vec{u}_e + \vec{V}\right) - K_e \vec{\nabla} T_e\right] = e\vec{f}_e.\vec{\nabla}\varphi - \mathrm{e}\sum_{\mathrm{i}} \Delta \mathrm{E}_{\mathrm{i}}^{\mathrm{e}} \mathrm{r}_{\mathrm{i}} + \frac{3}{2} k_B n_e \frac{2m_e}{m_{kb}}\left(T_e - T_g\right)\bar{\vartheta}_{e,kb} \tag{4.3}$$

Here e_e represents the internal energy of electrons given by $\frac{3}{2}n_e k_B T_e$, p_e is the partial pressure of electrons given by $n_e k_B T_e$, u_e is the electron convective velocity obtained from the drift diffusion approximation and K_e is the thermal conductivity. The source terms on the RHS represent the electron joule heating given by $e\vec{f_e}.\vec{\nabla}\varphi$, the inelastic collision source term given by -e $\sum_i \Delta E_i^e r_i$ (ΔE_i is the energy of electron impact reaction i and r_i is the rate of progress) and the elastic collision term due to collisions with the background species given by $\frac{3}{2}\, k_B n_e \frac{2m_e}{m_{kb}}\left(T_e - T_g\right)\bar{\vartheta}_{e,kb}$ where m_e is the mass of an electron and m_{kb} is the molecular mass of the background species. $\bar{\vartheta}_{e,kb}$ is the electron-background species collision frequency. To obtain the flux term in the species continuity equation for ions, the ion momentum equation is solved which is given by:

$$\frac{\partial n_i \vec{u}_i}{\partial t} + \vec{\nabla}.(n_i \vec{u}_i \vec{u}_i) = -\frac{e n_i}{m_i}\vec{\nabla}\varphi - \frac{k_B T_i}{m_i}\vec{\nabla} n_i - n_i\left(\vec{u}_i - \vec{V}\right)\bar{\vartheta}_{i,kb} \qquad (4.4)$$

This equation is obtained by taking velocity moment of the Boltzmann equation; the terms on the LHS represent the unsteady and inertial terms while the terms on the RHS represent the body forces due to the electric field, the pressure gradient terms and the momentum transfer collision source term.

The self-consistent electrostatic potential is obtained from the Poisson's equation given by:

$$\nabla^2\varphi + \frac{e}{\varepsilon_0}\sum_{k=1}^{K_g} Z_k n_k = 0 \qquad (4.5)$$

φ represents the electrostatic potential, e is the electronic charge and ε_0 is the permittivity of free space. Z_k represents the charge on species k (eg: +1 for single positive ions).

The species in the argon plasma comprises two metastable species Ar* and Ar_2*, two ions Ar^+ and Ar_2^+, electrons and the dominant background argon. The detailed chemistry and mobility calculations used in the model are described in (Deconinck, 2009) and (Deconinck, 2008). The ion diffusion coefficients are calculated using the Einstein relation,

$$D_k = \frac{k_B T_g \mu_k}{e Z_k} \qquad (4.6)$$

The coefficient of thermal conductivity that appears in the gas energy equation is calculated as $\eta_k = \frac{5}{2} n_k k_B D_k$.

Maxwellian flux of electrons is imposed at the walls of the thruster along with the secondary electron emission given by

$$\Gamma_e^{\,w} = \frac{1}{4} n_e \left(\frac{8 k_B T_e}{\pi m_e}\right)^{1/2} - \gamma_{eff}\Gamma_{ion}.\hat{n} \qquad (4.7)$$

Here $\hat{n}$ is the unit normal vector pointing towards the wall. γ_{eff} is the effective secondary electron emission coefficient. The second term on the RHS represents the

secondary electron flux. The ion flux is calculated based on mobility and the local electric field. It is assumed to be zero if the local electric field is pointing in direction opposite to the wall. A pure Maxwellian flux is imposed for all the neutral species at the wall. The electron energy flux at the wall is calculated as $Q_e^w = 2k_B T_e \Gamma_e^w$. The gas temperature is fixed to 300K at the walls.

The dielectric wall surfaces trap charge according to the equation given below. Charge trapping is the basic mechanism by which a dielectric barrier discharge is pulsed. The equation to calculate the boundary surface charge is given by:

$$\frac{\partial \rho_s}{\partial t} = \sum_{k=1}^{K_g} e Z_k \overrightarrow{\Gamma_k} . \hat{n}, \tag{4.8}$$

where ρ_s is the boundary surface charge density and $\hat{n}$ is the unit normal vector pointing towards the wall.

4.2 Flow Model

The bulk flow equations are solved on a 2D axi-symmetric, unstructured, cell-centered finite volume framework. The two dimensional form of the compressible Navier-Stokes equation is given by:

$$\frac{d\vec{U}}{dt} + \overrightarrow{\nabla}.\vec{F}_{inviscid} = \overrightarrow{\nabla}.\vec{F}_{visc} + S \tag{4.9}$$

Here $\vec{U}$ represents the four conservative variables for mass, momentum and energy, $\vec{F}_{inviscid}$ represents the inviscid flux term, $\vec{F}_{visc}$ represents the viscous flux term, and *S* represents the source term which is obtained from the plasma solver discussed in the subsequent section. The coefficient of viscosity varies with temperature according to Sutherland's law and the coefficient of thermal conductivity is calculated based on the Prandtl number. The electrostatic forces and collisions contribute to the momentum source term which is obtained from the plasma solver given by:

$$\vec{f} = \sum_i n_i(\vec{u}_i - \vec{V})\bar{\vartheta}_{i,k} - \frac{e n_e \vec{E}}{m_e} \tag{4.10}$$

Here n_i is the number density of species i, $\vec{u}_i$ the drift velocity and V_i is the bulk flow velocity. n_e and m_e are the number density and mass of electron respectively. E is the electric field. $\nu_{i,k}$ is the collision frequency of species i with the background neutrals.

The source term for the energy equation is given by:

$$S_{Heat} = -e\left(\sum_h Z_k(\vec{\Gamma}_k + n_k\vec{V}).\vec{\nabla}\varphi\right) + \frac{3}{2}k_B n_e \frac{2m_e}{m_{kb}}(T_e - T_g)\bar{\vartheta}_{e,k} - e\sum_{j=1}^{I}\Delta E_j r_j \tag{4.11}$$

The first term on the RHS in the energy source term is the Ion Joule heating, the second term is the contribution of elastic collisions of heavy species with electrons and the last term represents the energy transfer through inelastic collisions in the finite rate chemistry. ΔE_j is the enthalpy of reaction j in electron volts.

4.3 Plasma-Flow Coupling

First the compressible Navier Stokes equations are solved over the unstructured mesh to steady state. The steady state temperature, pressure and velocity distribution are determined. The thrust and specific impulse are also found out which will be referred to as the cold gas thrust and specific impulse. The temperature, pressure and velocity distribution is then used in the plasma solver as bulk flow parameters and the distribution of the steady state total energy source term is determined. The bulk flow Navier stokes equations are then solved with the total power deposition from the plasma as energy source term to obtain the new temperature, pressure and velocity distribution. The process is repeated to achieve a steady-state coupled plasma-flow solution.

5.0 MICRO-DBD SIMULATIONS

The design of the MCD thruster is based on the idea of covering the electrodes with a suitable refractory material to protect it from wear through ion bombardment and heating effects. The dielectric-covered electrodes along with a discharge gap on the order of micrometers constitute a system similar to a micrometer-scale Dielectric Barrier Discharge (micro-DBD). Therefore it is necessary to characterize the gas heating in these discharge systems. One dimensional plasma simulations are performed at constant pressure to characterize the heating source terms and the various discharge parameters in a micro DBD. Also a comparison with respect to gas heating is made with classic DBDs whose dimensions are on the order of millimeters.

5.1 Results

We choose a one-dimensional, parallel-plate geometry for both classic DBD and the micro DBD computational studies. The gas gap distance for the classic DBD is 2.5 mm and for the micro DBD is 50 μm. The gas gap is discretized by 100 mesh cells in both cases and is found to be adequate to provide mesh-converged solutions. In the case of the classic DBD it is assumed that the dielectric thickness covering both electrodes is 1.25 mm. In the case of the micro DBD a dielectric of thickness 25 μm is assumed to cover both electrodes. The relative permittivity of the dielectric is chosen to be 8 (similar to that of glass) for both discharges. For the results reported in this study, the coordinate axis starts from an electrode and therefore the gas gap extends from 25 μm to 75 μm for the micro DBD and from 1.25 mm to 3.75 mm for the classic DBD. The pressure is defined such that the *pd* product (pressure x gas gap distance) is the same for both the classic DBD and the micro DBD. The micro DBD is operated at atmospheric pressure (760 Torr) while the classic DBD is operated at 15 Torr; the *pd* product in both cases being the same value of 3.8 Torr-cm. We define a base case where both discharges are excited by a 500 V peak sinusoidal waveform applied at the electrode to the left while the electrode to the right is grounded. The AC frequency for the base cases are 10 MHz. Both discharges are therefore operated with the same nominal reduced electric field (*E/N*) condition. The initial temperature of the gas is set to 300 K for the both the discharge systems and the dielectric walls are kept at a fixed temperature of 300 K. Other conditions defined for the model include the ion Joule heating thermalization factor, which is set to 0.25 for the micro DBD and 0.8 for the classic DBD. Both values are based on the ratio of the ion mean free paths to the gas gap distances and the corresponding estimates for the thermalization factor is reported in literature (Deconinck, 2008).The above defined base cases are also modified to study the effect of frequency and voltages on classic and micro DBD discharge dynamics with a particular emphasis on understanding gas heating processes.

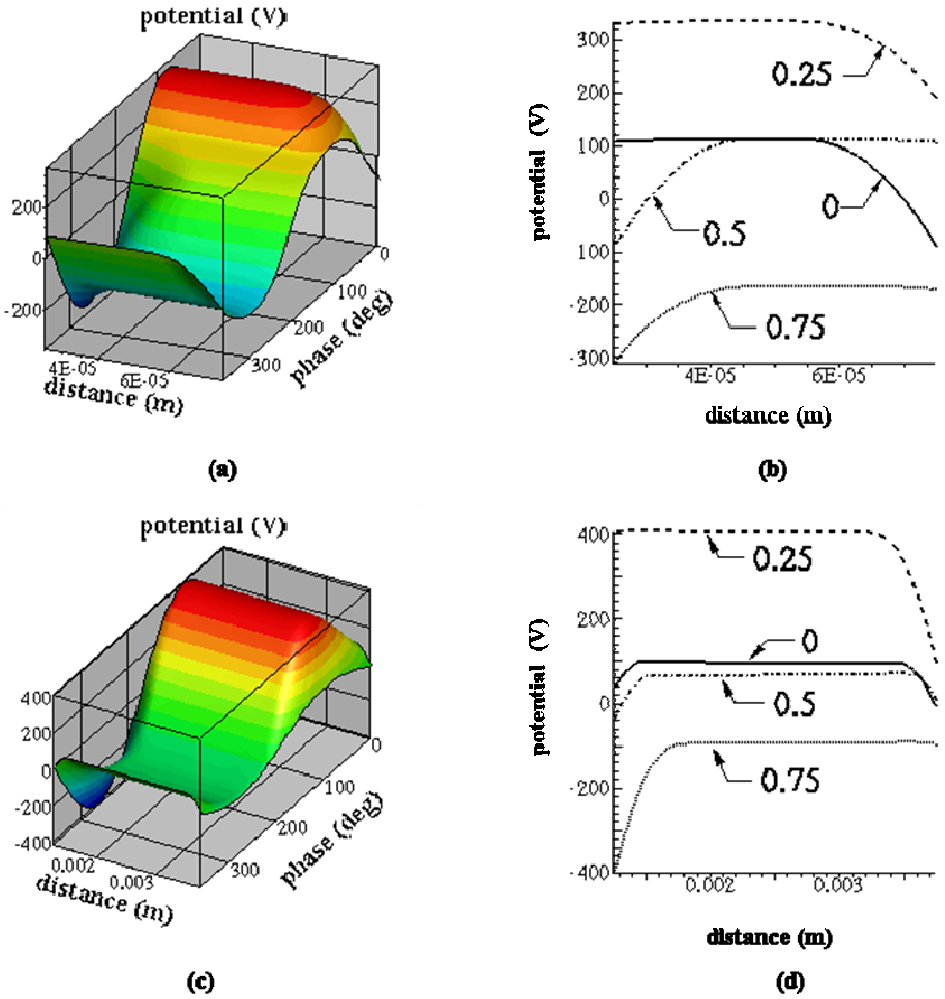

Figure 5.1: (a) Spatiotemporal variation of electrostatic potential in the micro DBD base case over a single AC cycle. (b) The electrostatic potential variation in the discharge gap at four time instances during the AC cycle in the micro DBD base case: 0 and 0.5 correspond to zero voltage at the electrode, 0.25 corresponds to the positive maximum and 0.75 corresponds to the negative maximum electrode voltage. (c) and (d) show the same information as in (a) and (b) for the classic DBD base case.

Figure 5.1 shows the spatiotemporal variation of the electrostatic potential in the classic and micro DBD discharges over a single cycle. The conditions correspond to the base case of 500 V peak and 10 MHz frequency. A periodic steady state in the current and voltage waveforms at the dielectric surfaces was nominally observed after 10-15 cycles and the plasma densities approach a periodic steady state after about 80 cycles. The potential variations in the plasma resemble a capacitively coupled plasma discharge with oscillating sheaths at the two bounding surfaces. The maximum sheath thickness seen in the micro DBD is about 40% of the discharge gap(Figure 5.1(c))and is smaller (~20%) in the case of the classic DBD(Figure 5.1(d)).Therefore a significant fraction of the micro DBD gap distance is non-neutral. The relatively large temporal variations in the value of the potential at the right dielectric surface adjacent to the ground electrode (200 V for micro DBD and 100 V for classic DBD), is owing to contributions from

surface charge trapping at the dielectric surface and the potential drop across the dielectric layer due to its capacitance.

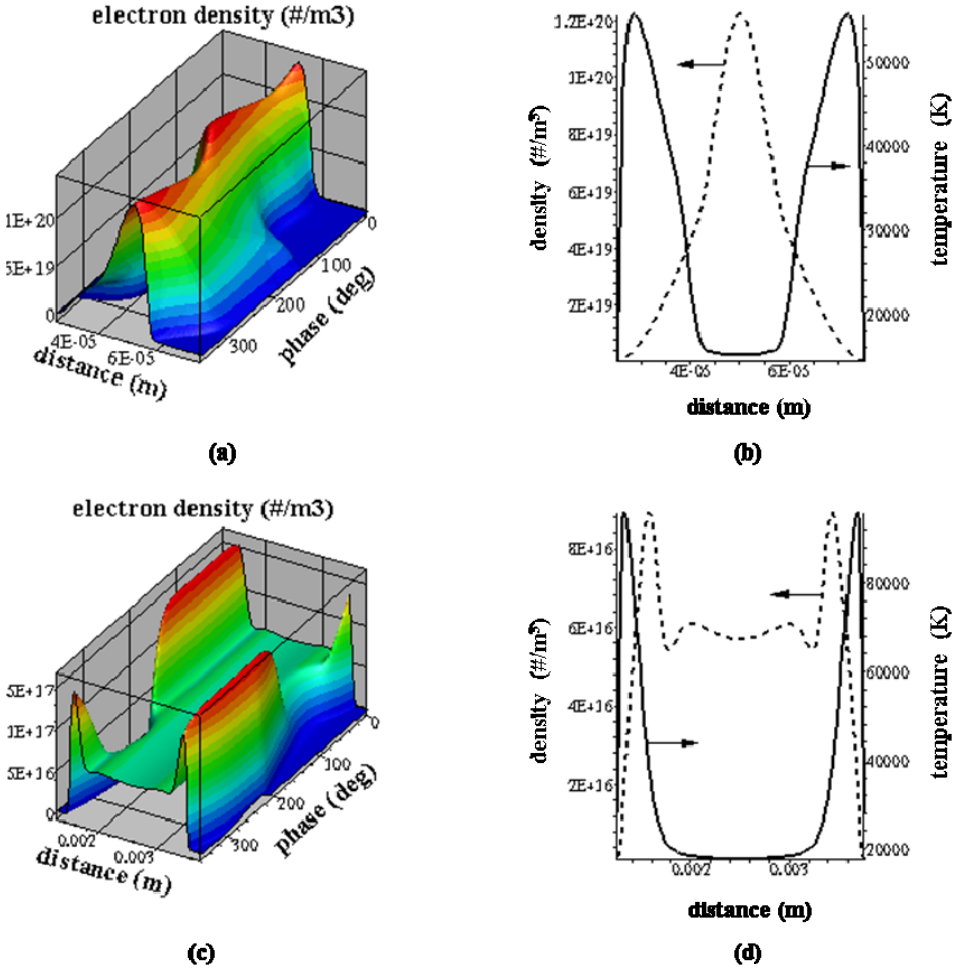

Figure 5.2: (a) Spatiotemporal variations of the electron density in the micro DBD base case over a single AC cycle for base case conditions. (b) Cycle averaged electron density and electron temperature in the micro DBD base case. (c) and (d) show the same information as in (a) and (b) for the classic DBD base case.

Figure 5.2(a) and Figure 5.2(c) show the spatiotemporal variations of the electron density in the micro DBD and classic DBD, respectively, over a single AC cycle and Figure 5.2(b) and Figure 5.2(d) shows the corresponding time-averaged electron density and electron temperature for the same cases. Peak electron densities of about 1.2×10^{20} m^{-3} are seen at the center of the discharge for the micro DBD case. Since the gap is mostly non-neutral with the sheaths occupying most of the discharge, the location and magnitude of the peak electron density varies significantly during the cycle. The electron densities are much lower (~10^{16} m^{-3}) in the classic DBD case but the sheath thickness is a much smaller fraction of the gas gap distance resulting in a well-defined bulk plasma region. For this case, the electron densities in the bulk plasma remain steady through the cycle at a nearly uniform value of about 6×10^{16} m^{-3}.In the sheath region, large temporal variations are observed in the electron densities, with peak

densities of about $5x10^{17}$ m^{-3} observed during the local anodic phase of the dielectric surfaces.

Electron volumetric generation occurs through five different pathways in the high-pressure argon chemical reaction mechanism used in this study (Deconinck, 2009). Electron-impact ionization of neutrals (Ar) and metastable argon (Ar*), Penning ionization of Ar*, Penning ionization of Ar_2* and electron-impact ionization of Ar_2* are the important pathways. For the lower pressure classic DBD case, the electron-impact reactions are the primary source of electrons. The higher pressure in the micro DBD case favors three-body collision reactions which results in the formation of dimer species of argon. These in turn give rise to larger generation of electrons. As seen in Figure 5.2(b), the cycle-averaged electron temperatures are of the order of 1 eV in the bulk plasma and rises to a value of ~ 6 eV in the sheath region in the case of the micro DBD case. A similar trend is observed in the case of the classic DBD as well, with cycle-averaged electron temperature of about 2 eV in the bulk and 9 eV in the sheath region. A sharp rise in the electron density is seen close to the sheath edge in Figure 5.2(d) is due to electron generation through electron-impact ionization brought about by high energy secondary electrons from the wall. This rise in electron density near the sheath is not observed in the micro DBD case due to the much larger extent of the sheath region (that covers a significant portion of the discharge gap) and electron generation through other pathways that include dimer argon species.

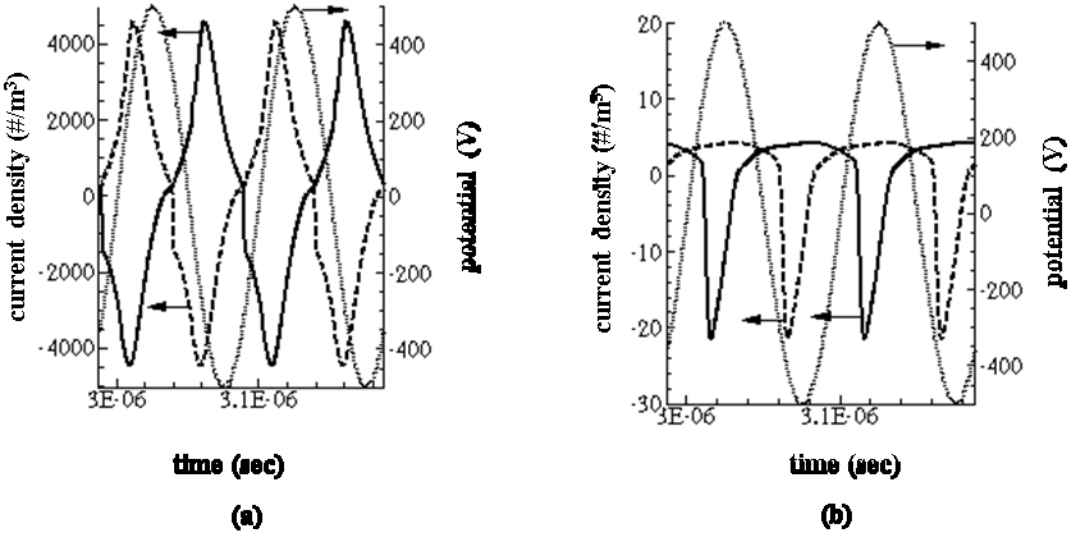

Figure 5.3: (a) Conduction current densities at the powered (solid line) and grounded (dashed line) dielectric surfaces for the micro DBD base case. (b) Same information as (a) for the classic DBD base case. The dotted line represents the base case applied voltage waveform at 500V, 10MHz. (Note that the conduction current density direction is assumed positive towards the respective surfaces).

Figure 5.3(a) and Figure 5.3(b) show the applied voltage at the powered electrode and conduction current density waveforms at the powered and grounded dielectric surfaces, respectively. The displacement current itself is nearly sinusoidal with the corresponding AC frequency. It is observed that the conduction current densities in the micro DBD reach about 4000 mA/cm^2 and is much higher than the 20 mA/cm^2 in the classic DBD

case. In the positive half cycle, the powered dielectric behaves like an anode and the conduction current at this electrode results predominantly from electrons while in the negative half cycle conduction current at the powered dielectric is due to ions. The ion and electron current densities are found to be comparable in magnitude for the micro DBD case, resulting in relatively symmetric conduction current pulsing at a dielectric surface every half cycle (see Figure 5.3(a)). For the classic DBD case the ion current densities are much smaller than the electron current densities resulting in a highly asymmetric current pulsing at a dielectric surface. The large differences in the conduction current waveforms between the micro DBD and the classic DBD can be understood as follows. During the positive half cycle of the applied voltage waveform the powered dielectric surface behaves like an anode while the grounded dielectric surface behaves like a cathode. During this phase, the conduction current at the powered dielectric surface is predominantly due to electron flux to the surface, while the conduction current at the grounded dielectric surface is due to the ion flux (Ar^+ and Ar_2^+). For the micro DBD case, the ion density at the grounded dielectric surface is high enough to yield ion fluxes comparable to the electron flux at the powered dielectric surface. The high ion densities are a result of operation at higher pressures and due to an increase in the local reduced electric field in the plasma sheath, owing to lower background number density brought about by gas heating. A similar argument can be made during the negative half cycle of the applied voltage waveform as well. The consequence is that the ion current at the anodic surface is comparable to the corresponding electron current at the cathodic surface during any given time in the cycle. Overall, the magnitudes of currents at the two dielectric surfaces are nearly the same at any time instance during the cycle.

The cycle averaged ion and metastable species densities are shown in Figure 5.4. As mentioned earlier, three-body collision reaction rates are significant under the high pressure conditions of the micro DBD case and less important for the lower pressure classic DBD case. Consequently, the dimer Ar_2^+ ions are the dominant ion species in the center of the micro DBD (Figure 5.4(a)). The dimer ions are less important in the classic DBD, although they do appear in relatively significant amounts even for the classic DBD (Figure 5.4(b)). Overall, the ion densities are about two orders of magnitude higher in the micro DBD compared to the classic DBD. Figure 5.4(c) and Figure 5.4(d) show cycle averaged metastable species density in the micro and classic DBDs, respectively. The monomer Ar* metastable is the dominant radical in both the discharges although the relative concentration of the dimer metastable Ar_2^* to the monomer metastable is much higher in the micro DBD case compared to the classic DBD. We note that similar high densities of dimer ion and metastable species are reported in high-pressure DC microdischarges (Deconinck, 2009).

The gas temperature increase in the discharge depends on the ion Joule heating, energy gained by heavy species due to elastic collisions with electrons and energy gained or lost through inelastic collisions in the plasma. These quantities appear as the source terms in the gas temperature Eqn. (4.5). Figure 5.5(a) and Figure 5.5(c) show the spatiotemporal variation of total power density in the micro and classic DBD, respectively. Figure 5.5(b) and Figure 5.5(d) show the cycle averaged values of each of

the individual gas temperature source terms for both discharges. The ion Joule heating is observed to be the dominant source term in both the discharges. Furthermore the ion Joule heating is dominant in the sheath regions of the discharges owing to the high electric fields. It is also clear that the gas heating source term in the micro DBD is about four orders of magnitude higher than the classic DBD case. In the center of the discharge the inelastic collision source term (resulting from Penning ionization, metastable de-excitation and charge transfer reactions) play an important role although the magnitude of this term is about an order of magnitude lower than the ion Joule heating term in the micro DBD and about three orders lower than the ion Joule heating in the classic DBD.

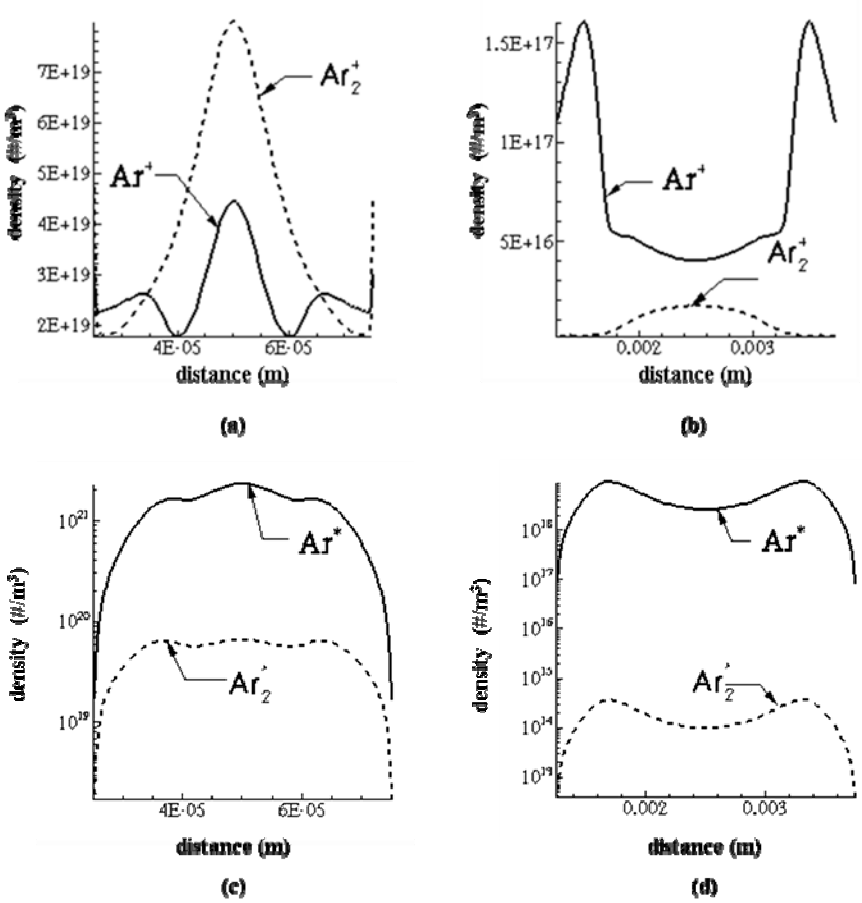

Figure 5.4: (a) Cycle-averaged ion densities in the plasma for micro DBD base case and (b) for classic DBD base case, respectively. (c) Cycle-averaged metastable densities in the plasma for the micro and (d) for classic DBD base cases, respectively.

The gas temperature rise in both the discharge systems result from a competition between volumetric gas heating and thermal conduction wall losses at the boundaries. The gas heating source density is significantly higher in micro DBDs, but the much smaller length scales also mean that conductive losses are higher resulting in lower gas temperatures. The overall balance between these competing processes determines the magnitude of gas temperature increase in the discharge gap. Figure 5.6 shows the spatiotemporal variations and the cycle averaged gas temperature profiles in both

discharges. Recall that the wall temperature is fixed at 300 K for all cases. Local peaks are observed in the gas temperature every half cycle in the sheath region for both the micro and classic DBD cases. This peak in the sheath region corresponds to the location of the ion Joule heating. The micro DBD experiences larger gas temperature excursions per half cycle of ~ 400 K compared to the classic DBD case where per half cycle excursions are of ~ 80 K.

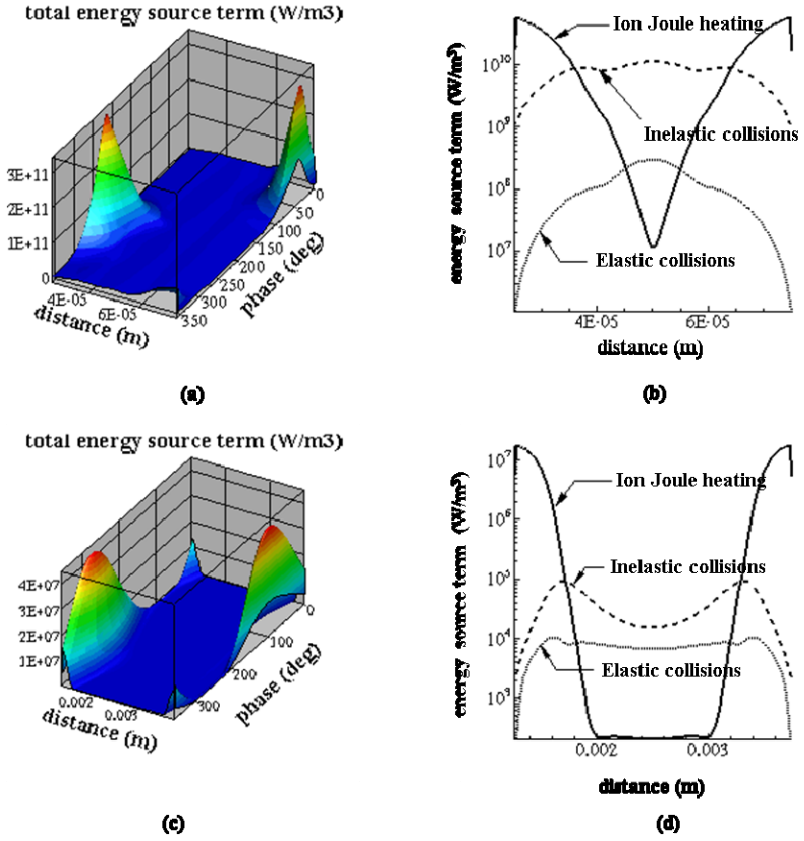

Figure 5.5: (a) Spatiotemporal variations in the total gas heating source term over a single cycle of the excitation voltage waveform for the micro DBD base case. (b) Profiles of the individual cycle averaged gas heating source terms for the micro DBD base case. (c) and (d) provide the same information as (a) and (b), for the classic DBD base case.

Moreover, there is appreciable change in temperature in the bulk of the plasma as well for the micro DBD case due to the relative large sheath thickness and the larger contribution of inelastic and elastic collision source terms that are significant at the center of the discharge. The cycle averaged gas temperatures are shown in Figure 5.6(c) for the micro and classic DBDs. Note that the x axis in Figure 5.6(c) is the non-dimensional gap distance which is the ratio of the location in the one dimensional domain of a particular DBD to its discharge gap distance. The averaged gas temperature increase peaks at the center for both cases and is much larger for the micro DBD (~250 K) compared to the classic DBD (~ 25 K). The large temporal variations in gas temperature on the time scales of a single AC cycle are somewhat surprising given the relatively large AC frequency of 10 MHz. These variations can however be explained based on the characteristic time scales for gas heating and cooling in the discharges compared to the time scale of a single AC cycle. The

characteristic time scale for gas heating (τ_h) depends on the thermal capacity of the gas (density times the specific heat, ρC_p), the characteristic temperature increase (ΔT), and the magnitude of the volumetric source term (S) and is expressed as $\tau_s = \rho C_p \Delta T/S$. Taking argon gas density as 1.6 kg/m^3 at atmospheric pressure, specific heat of argon as 520 J/kg-K, a characteristic temperature increase of 10 K, and volumetric source of 10^{11} W/m^3, the characteristic time scale for gas heating is ~ 10^{-7} s. Gas cooling is a consequence of thermal conduction in the inter-dielectric gap. Characteristic time scale for gas cooling (τ_c) is given in terms of the gap distance (l), the thermal capacity (ρC_p), and the gas thermal conductivity (k) as $\tau_D = l^2 \rho C_p/k$. Taking the distance between the characteristic sheath heating location and the adjacent wall as the characteristic length scale (~ 10^{-6} m), and a thermal conductivity for argon as 1.6 W/m-K, the characteristic cooling time scale is also ~ 10^{-7} s. Both gas heating and cooling time scales are comparable to the AC cycle time scale of 10^{-7} s, explaining the large temporal variations in the gas temperature in the micro DBD case. Similar estimates can be made to explain the gas temperature variations in the classic DBD case.

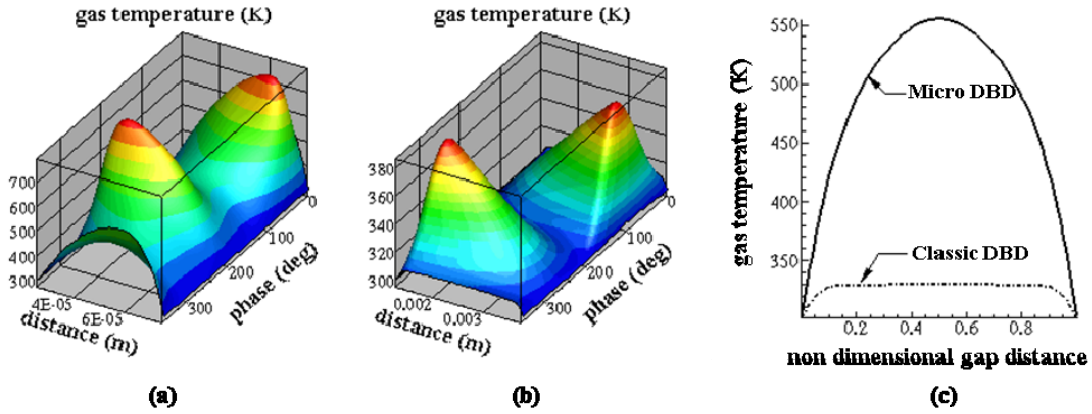

Figure 5.6: (a) and (b) show the spatiotemporal variation of gas temperature over a cycle in the micro and classic DBD base cases, respectively. (c) shows cycle averaged gas temperature in the discharge for the base cases.

We now study the sensitivity of micro DBD gas heating to changes in the drive voltage and the excitation frequency. Figure 5.7(a) shows the cycle averaged gas temperature profiles in the micro DBD as a function of changes to the applied waveform voltage at 500 V, 1000 V, and 1500 V. Increasing voltage results in an increase in the power deposition into the gas through ion Joule heating and a corresponding increase in the gas temperature from peak value of about 550 K at 500 V to about 1400 K at 1500 V.

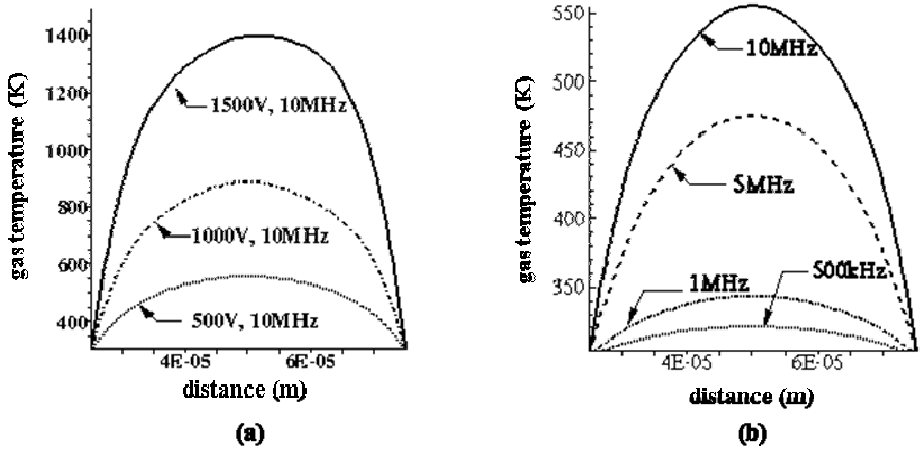

Figure 5.7: (a) Cycle averaged gas temperature profiles in the micro DBD for varying applied AC voltage at a fixed 10 MHz frequency. (b)Cycle averaged gas temperature profile in the micro DBD for varying AC frequencies at a fixed AC voltage of 500 V.

Figure 5.7(b) shows the effect of changes to the AC frequency for a fixed AC voltage of 500 V. The frequency is varied from 500 kHz at the lower end to the base case of 10 MHz. The cycle averaged gas temperature shows a steady increase with increasing frequency. The reason for this trend is apparent from a careful look at the discharge dynamics at the lowest frequency of 500 kHz as shown in Figure 5.8. Figure 5.8(a) shows spatiotemporal variations in the electrostatic potential in the discharge during a cycle. During most of the cycle time period, the electrostatic potential profile between the dielectric surfaces is linear (dashed lines in Figure 5.8(a)), indicating a near vacuum potential during most of the time of a cycle. At brief instances during each half cycle, the linear potential is perturbed by strong pulsed discharge activity (solid lines in Figure 5.8(a)). The pulsed nature of the discharge is clearly seen in Figure 5.8(c), where the applied voltage waveform and the conduction current density at the powered and grounded dielectric surfaces are shown. The pulsed discharge results from the charging/discharging dynamics at the dielectric surfaces as discussed earlier, and have a characteristic pulse width that is relatively independent of cycle frequency (Shin, 2003), i.e. while the cycle time period increases with decreasing AC frequency, the pulse widths remain nearly the same as in the higher frequency excitation cases.

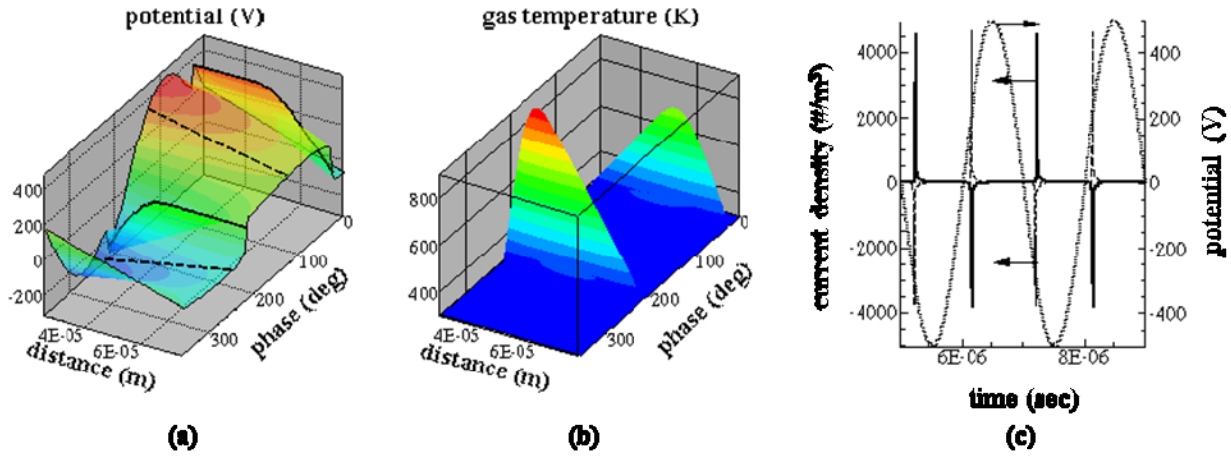

Figure 5.8: (a) Spatiotemporal variation of electrostatic potential in the plasma for the 500V, 500 kHz case. (b) Gas temperature spatiotemporal variation over a single cycle. (c) Conduction current densities at the powered (solid line) and grounded (lighter solid line) electrodes, the dotted line represent the applied voltage waveform.

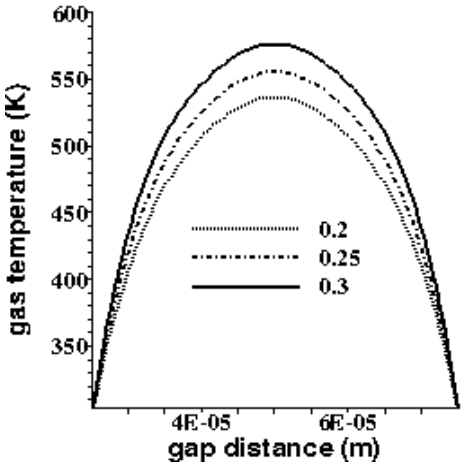

Figure 5.9: Sensitivity of the cycle averaged gas temperature profiles in the micro DBD to the ion Joule heating thermalization factors.

Figure 5.8(b) shows the spatiotemporal variation of the gas temperature in the discharge. Gas temperature excursions are observed during the narrow pulsed discharge events every half cycle, with the peak gas temperatures comparable to the higher frequency cases at the same voltage. Between pulses the gas temperature rapidly decreases to the fixed wall temperature value of 300 K. The overall trend of a steady increase in the cycle averaged gas temperature with increasing frequency is simply an integration effect of the fraction of time for rapid gas temperature excursion during the pulses compared to the total time period of cycle. For the low frequencies, the pulse time (high gas temperature time) is a very small fraction of the cycle time period. At the higher frequencies the pulse width is comparable to the cycle time period with a consequent increase in the cycle averaged gas temperature even though the peak gas temperature during a pulse is nearly independent of the frequency. The ion Joule heating thermalization factor (α_J) in Eqn. (4.5) is an important model constant that has a large impact on the gas temperature profiles in the discharge. We now determine the sensitivity of the cycle averaged gas temperatures to this parameter. Figure 5.9

shows the sensitivity of cycle averaged gas temperature in the micro DBD for varying ion Joule heating thermalization factors for the base case discharge conditions. As discussed earlier, only a fraction of the energy gained by the ions due to the electric field is thermalized with the background gas which is represented by the thermalization factor, (α_J) and the value of 0.25 chosen for this work is based on studies in the literature. A change to this factor by a relatively large amount of 0.05 (20% of 0.25), results in a $\pm$20 K change in the peak cycle averaged gas temperature, i.e. about 10 % change in the temperature increase. This relatively large sensitivity underscores the importance of an accurate estimate for the ion Joule heating thermalization factor in the model. Regardless, the model does provide a clear description of gas heating phenomena in micro and classic DBD discharges.

5.2 Conclusions

A multi species, multi-temperature, self-consistent plasma model was used to study discharge phenomena micro DBD with emphasis on understanding gas heating in these discharges. The study is facilitated by a direct comparison with classic large volume DBDs. Micro DBDs are characterized by significantly higher plasma and power densities compared to classic DBDs. At the same *pd* (pressure x discharge gap distance) and applied voltage waveform (500 V, 10 MHz), there is larger cycle-averaged gas temperature rise seen in the micro DBD ~ 250 K compared to smaller rise ~ 25 K in the classic DBD. It is also observed that the cycle-averaged gas temperature reduces as the operating frequency of the applied voltage waveform is reduced for the micro DBD case. Also, operation at higher voltage amplitudes yields higher gas temperature rise for the micro DBD case. The sensitivity of gas temperature to an important model parameter, the ion Joule heating thermalization factor, is also quantified. Specifically, a 20% change in the thermalization factor results in a peak gas temperature change of about 10 %. Overall, we conclude that high gas temperatures are achievable in micro DBDs, with higher cycle-averaged temperatures being favored for high frequency operation. Micro DBDs are therefore excellent device candidates to provide controllable gas heating in a variety of micro-electro mechanics systems.

6.0 TWO DIMENSIONAL SIMULATIONS OF THE MCD THRUSTER

From the one dimensional simulations it is clear that micro DBDs can bring about effective gas heating compared to millimeter length scale DBDs. Two dimensional simulations of the discharge in the MCD thruster is performed on an actual thruster geometry by coupling the plasma and the flow phenomena. The geometry and computational mesh used for the MCD thruster simulation is shown in Figure 6.1(a). The channel and nozzle exit diameters are 100 and 300 μm respectively. The channel section is 560 μm in length while the nozzle length is 140 μm. The electrodes are 160 μm apart. The dielectric thickness that separates the electrodes from the gas is 40 μm. The computational mesh has approximately 7000 cells in the channel section, 1700 cells in the nozzle and about 8000 cells in the dielectric section. The bulk flow Navier Stokes equations are solved in the gas subdomains (channel and nozzle section) while the plasma governing equations are solved only in the channel section for faster computation. Only the electrostatic Poisson's equation is solved in the dielectric subdomain. The base case applied voltage waveform for the case shown below is at 600 V amplitude with 10 MHz frequency. A comparative study of power deposition will be made with the above mentioned amplitude and varying frequency. The total pressure and total temperature at the inlet is 40 kPa and 300 K, respectively. The wall temperatures are fixed at 300 K. A very low pressure of 10 Pa is imposed at the exit plane. The cold flow pressure, velocity and temperature distribution is found out by solving the bulk flow Navier-Stokes equations without the plasma solver. The bulk flow parameters are used in the plasma module to study the evolution of various species in the plasma and the steady cycle-averaged power deposition is determined. Figure 6.1(b) shows the cold gas pressure distribution in the thruster. The pressure decreases as the flow accelerates through the channel section. A peak velocity of about 400 m/s is seen at the exit of the nozzle section as indicated by Figure 6.1(c). Figure 6.1(d) shows the temperature distribution in the channel and nozzle section. The temperatures remain close to wall temperature in the boundary layer while it is lower close to the axis due to isentropic cooling in the bulk flow. The cold flow pressure, temperature and velocity distribution is used in the plasma solver to study the evolution of various species in the plasma and also for the computation of the steady state power deposition into the background neutral gas. The steady current-voltage waveform is shown in Figure 6.2. Current densities ~ 700 mA/cm^2 are seen indicating high power densities in the plasma. The voltage waveform shown here is the potential at the center of the powered dielectric section shown in Figure 6.1(a). In the positive half cycle of the applied voltage waveform, the powered

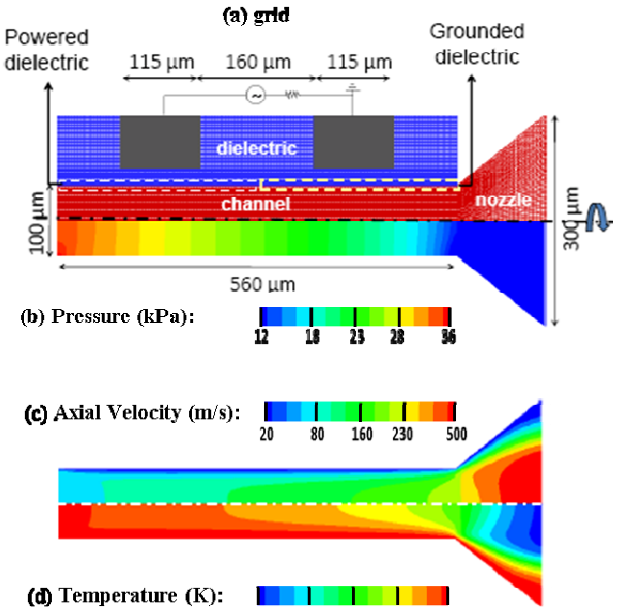

Figure 6.1: Computational grid and flow parameters.

dielectric section is anodic while the grounded dielectric is cathodic. The conduction current at the anodic section will be predominantly electron current while it will be ion current at the cathodic section. It is seen that the electron and ion currents at the dielectric sections are comparable. Figures 6.3(a) and 6.3(b) show the cycle averaged Ar^+ density and electron density in the channel section respectively. Number density ~ $3x10^{19}$ m^{-3} is seen in the bulk of the discharge. The ion densities are much higher in the oscillating sheath region close to the electrodes.

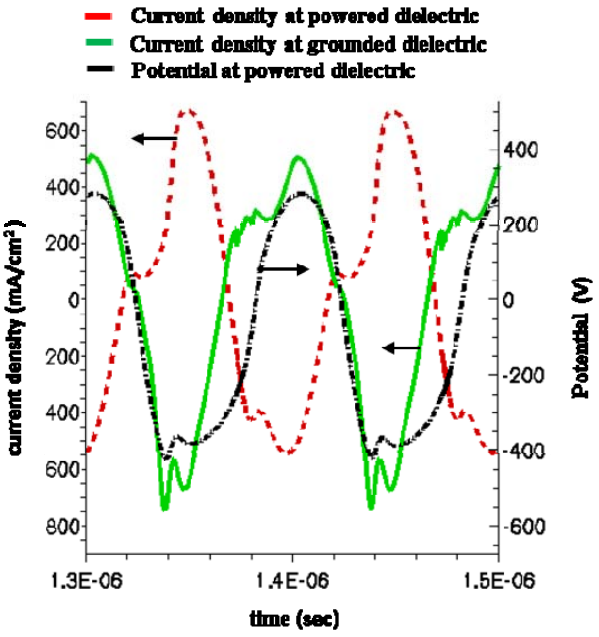

Figure 6.2: Current and voltage waveforms.

The electrons in the plasma are confined between the oscillating RF sheaths. Thus electron densities are seen to be higher in the bulk of the discharge. The dominant ionic species seen in the discharge is Ar^+ while the dominant metastable species is Ar*. Figure 6.3(c) shows the cycle averaged number density of the dominant metastable, Ar*. Peak number density ~ $2x10^{21}$ m^{-3} is seen in the bulk of the discharge. Ar* is mainly formed through electron-impact excitation. The electron densities are higher in the bulk of the discharge which help in bringing about excitation of the dominant background Ar. Figure 6.3(d) shows the cycle averaged electron production rate in the channel section. The production of electrons mainly happens through electron-impact ionization of neutral Ar and through penning ionization reactions. Therefore the peak production rates are observed in regions of high Ar* and Ar^+ densities. The total power deposition into the neutral gas is a combination of the ion Joule heating, energy transfer through inelastic collisions in the plasma and through elastic collisions of electrons with the neutral species. Figures 6.4(a) and 6.4(b) show the distribution of cycle-averaged heating through elastic and inelastic collisions, respectively. The elastic collision source terms peak in the regions of high electron densities while the inelastic collision source term is highest at regions with high excimer (Ar_2*) and metastable argon (Ar*) densities. The inelastic heating is seen to happen in the bulk of the plasma mainly due to excimer de-excitation and penning ionization reactions.

Figure 6.4(c) shows the cycle-averaged ion Joule heating in the discharge. It is seen that the ion Joule heating is two orders of magnitude larger than elastic heating and an order of magnitude larger than inelastic heating. Ion Joule heating is predominant in the oscillating sheaths owing to higher electric fields. The asymmetry in the ion Joule heating is due to the pressure distribution shown in Figure 6.1. Neutral densities are higher near the upstream dielectric surface resulting in higher ion densities and larger ion Joule heating. Figure 6.4(d) shows the cycle averaged total energy source term.

The total energy source term is almost entirely due to ion Joule heating. The integrated cycle-averaged power deposition through ion Joule heating is 46 mW which is about 75% of the total power supplied of 62 mW. The integrated inelastic and elastic heating is about 3 mW and 0.5 mW, respectively.

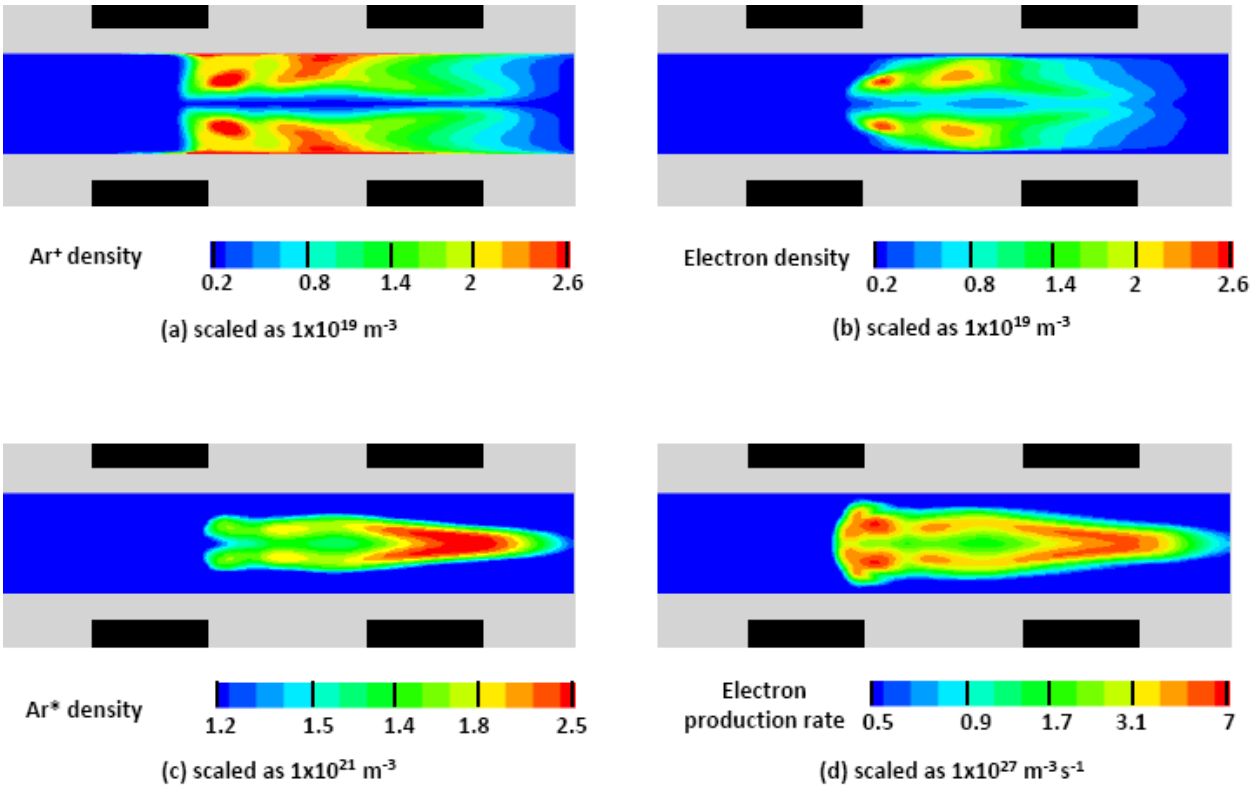

Figure 6.3: Number densities of various species and electron production rate.

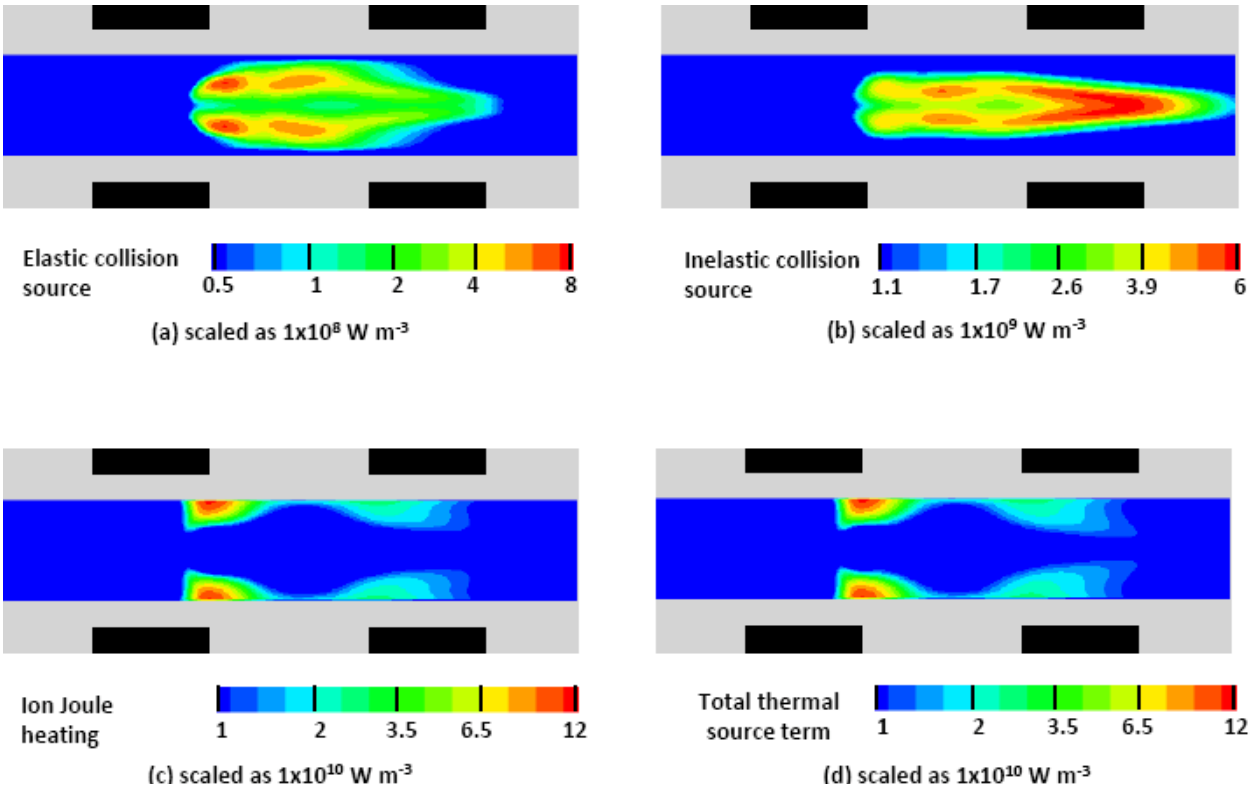

Figure 6.4: Gas energy source terms.

6.1 Effect of Addition of N_2

The results above indicate that the contribution to overall heating through inelastic collision source terms are very small compared to the ion Joule heating. It is also seen that the inelastic collision terms are dominant close to the axis which favors effective gas heating. To improve upon the contribution of inelastic collisional heating, a small amount of N_2 (20%) is mixed along with the propellant gas (Ar). The various excited states of nitrogen have been extensively studied in literature (Phelps, 1985), (Cartwright, 1977), (Mahadevan, 2010) and the collisional de-excitation of these species will contribute to the inelastic source term. To incorporate the presence of nitrogen in the discharge, the pure argon chemistry has been modified by the following reactions shown below in Table 6.1. Here T_e is the electron temperature in eV.

Table 6.1: Additional finite rate Ar-N_2 reactions

#	Reactions	Reaction Rate (cm, #, s)
G1	$e + N_2 \rightarrow N + N + e$	$1.959 \times 10^{-6}\ T_e^{-0.7}\ \exp(-9.75/T_e)$ (Yuan, 2003)
G2	$e + N_2^+ \rightarrow N + N$	$2.54 \times 10^{-6}\ T_e^{-0.5}$ (Yuan, 2003)
G3	$e + N \rightarrow N^+ + 2e$	$8.401 \times 10^{-5} \exp(-14.5/T_e)$ (Yuan, 2003)
G4	$e + N_2 \rightarrow N_2^+ + 2e$	$4.483 \times 10^{-7}\ T_e^{-0.3} \exp(-15.6/T_e)$ (Yuan, 2003)
G5	$2e + N_2^+ \rightarrow N_2 + e$	$5.651 \times 10^{-27}\ T_e^{-0.8}$ (Yuan, 2003)
G6	$e + N_2 \rightarrow N_2^* + e$	From offline Boltzmann solver BOLSIG+ (Mahadevan, 2010)
G7	$Ar^+ + N_2 \rightarrow Ar + N_2^+$	5.0×10^{-10} (Moravej, 2006)
G8	$Ar^* + N_2 \rightarrow Ar + N_2^*$	13.14×10^{-11} (Moravej, 2006)

Since nitrogen has more than 20 excited states, the species themselves are not modeled in the chemistry outlined in Table 6.1 for faster computation. We model only the energy transfer that happens in the excitation and de-excitation process. The details regarding how this is done is given in (Mahadevan, 2010). The reaction G6 represents the electron impact excitation of nitrogen molecule where energy is lost from the electron pool.

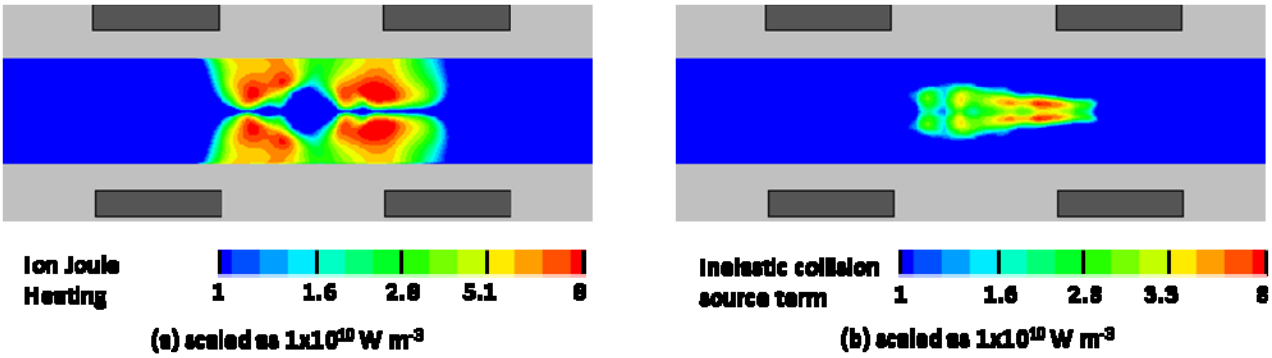

Figure 6.5: Gas energy source terms in Ar-N_2 discharge.

The collisional de-excitation of nitrogen (predominantly due to collision with background neutrals) adds energy to the heavy species pool. The energy transfer into the heavy species pool due to de-excitation of vibrationally excited species is not considered. This is because the residence time of the vibrationally excited states of nitrogen is on the order of milliseconds (Vincenti, 1965) while the flow time scales here are on the order of microseconds. Therefore these species are convected out of the thruster before they can de-excite and transfer energy into the heavy species pool. Simulation studies were done on the same geometry as shown in Figure 6.1, the only change being the use of 80% argon and 20% nitrogen as propellant gas. The applied voltage waveform used for this case is at amplitude of 800 V and 10 MHz. The voltage amplitude chosen is higher compared to the base case because of higher breakdown voltages seen for the Ar-N_2 mixture compared to the pure argon case. This has been observed in experiments performed on micro cavity discharges as well. Figure 6.6 shows the cycle-averaged ion

Joule heating and inelastic collision source term in the discharge. It is seen that the magnitude of inelastic collision source terms have increased considerably. The integrated ion Joule heating contributes to about 88% of the total power deposition while inelastic collision source term contributes to about 12%. The contribution of inelastic collisions in the pure argon case was about 6%. Therefore addition of nitrogen into the discharge has significantly enhanced the power deposition through inelastic collisions.

6.2 Effect of Frequency

Operation of the discharge at a higher frequency of 20 MHz results in higher plasma densities and spatially dominant sheaths compared to the 10 MHz case, as shown in Figure 5. Figures 6.5(a) and 6.5(b) show the cycle averaged electron densities for the discharge at 10 MHz and 20 MHz frequency, respectively. The amplitude of the applied voltage waveform is kept at 600 V for both the cases. High electron densities are observed close to the axis for the 20 MHz case. Due to rapidly oscillating sheaths at higher frequencies, the electrons are confined in the bulk of the discharge resulting in greater plasma densities.

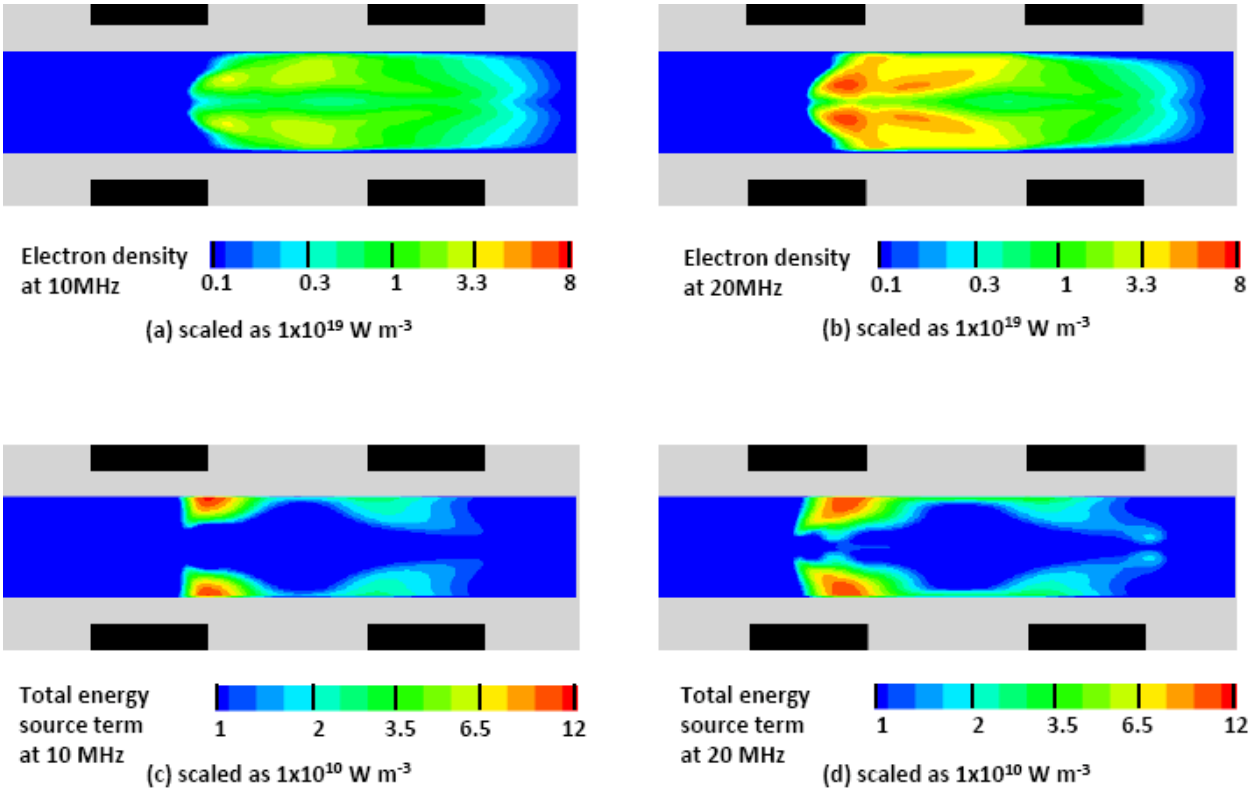

Figure 6.6: Electron density and total energy source term for varying frequency.

Figures 6.5 (c) and 6.5(d) show the cycle averaged total energy source terms in the discharge for the 10 MHz and 20 MHz case, respectively. The dominant heating mechanism is again through ion Joule heating which is dominant in the sheath region. The ion Joule heating seems to spread out more towards the axis in the 20 MHz case.

The integrated ion Joule heating is also seen to be higher for the 20 MHz excitation (~64 mW) compared to the 10 MHz case (46 mW).

6.3 Thruster Performance Calculations

The averaged total power deposition is used as energy source term in the bulk flow Navier-Stokes equations to obtain the enhancement in thrust and specific impulse. Figures 6.6 (a) and 6.6(b) show the temperature distribution in the neutral gas flow for the 10 MHz and 20 MHz RF excitations, respectively. The top half of both the figures shows the temperature profile for the cold gas case. Peak temperature rise ~160 K is seen close to the wall after power deposition for the 20 MHz case.

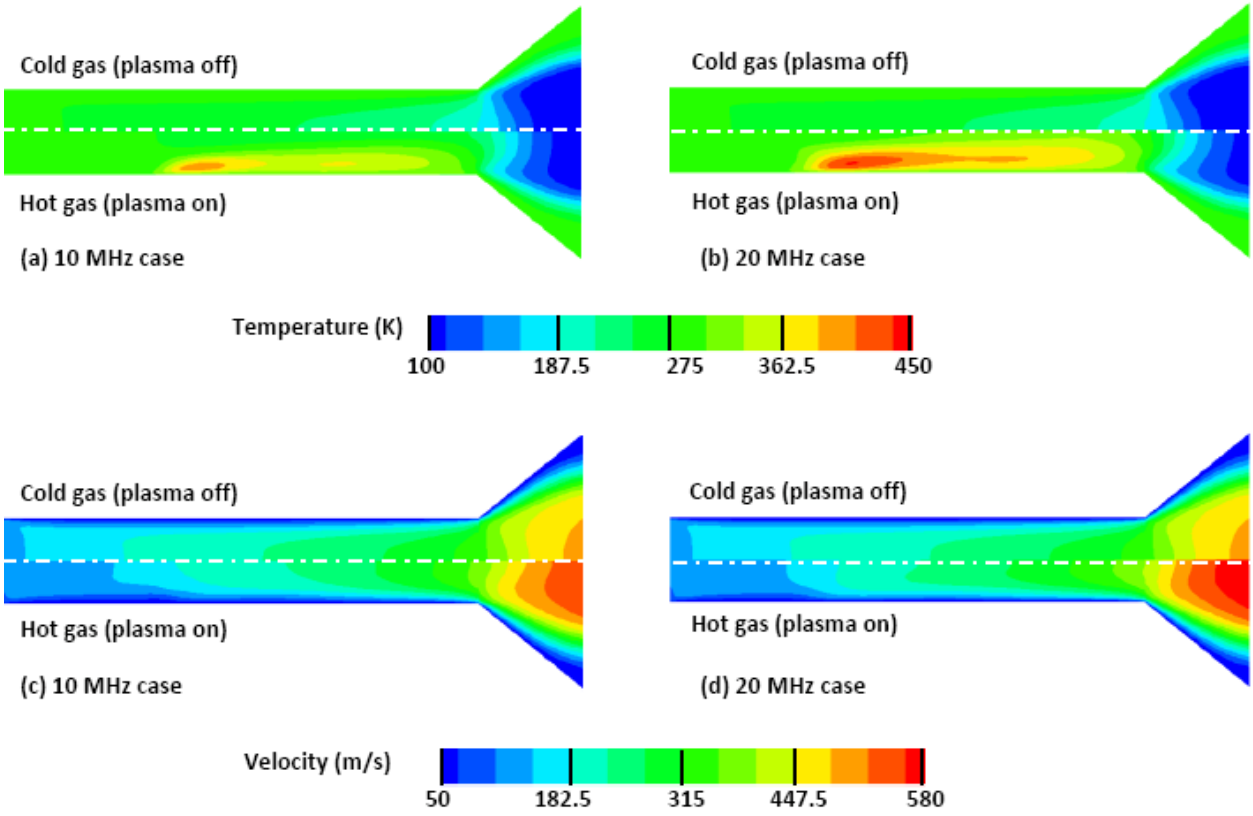

Figure 6.7: Comparison of cold and hot gas temperature and velocities for varying frequencies.

Table 6.2: Comparison of various performance parameters.

Case	Mass flow rate (kg/s)	Integrated thermal source term (mW)	Thrust (uN)	Specific Impulse (sec)
Cold gas	5.5×10^{-7}	0	299	55
Hot gas (10 MHz)	4.5×10^{-7}	50	269	61
Hot gas (20 MHz)	4.4×10^{-7}	68	278	65

There is larger gas heating observed in the 20 MHz excitation, due to higher cycle-integrated thermal source term. Figure 6.6(c) and 6.6(d) show the axial velocity

distribution for the 10 MHz and 20 MHz case, respectively. A peak velocity ~ 600 m/s is seen at the exit plane for the 20 MHz compared to ~ 500 m/s in the case of the cold gas thruster. Table 6.1 summarizes the various performance parameters for the different cases discussed above.

The thrust is calculated based on the pressure and axial velocity at the exit plane as shown in the equation below. The specific impulse is calculated as the ratio of the thrust to the mass flow rate times the acceleration due to gravity as shown below.

$$T = \int_0^R (P + \rho V_{ax}^2)(2\pi r)dr \tag{6.1}$$

$$I_{sp} = \frac{T}{\dot{m}g} \tag{6.2}$$

The mass flow rate tends to reduce after addition of heat in the channel section. This is due to the increase in stagnation temperature while keeping the stagnation pressure a constant. Thrust also reduces after heat addition but the specific impulse for both the hot gas cases is higher than the cold gas. A specific impulse enhancement ~ 10 sec is observed for the 20 MHz case.

6.4 Conclusions

The discharge phenomenon in a micro cavity discharge thruster has been simulated using a continuum fluid model. The cycle-averaged thermal energy source terms are obtained by solving the plasma governing equations which are then coupled with the Navier-Stokes model to obtain enhancement in specific impulse. The operation of the thruster using an alternating current waveform of amplitude, 600V with varying frequency (10 MHz, 20 MHz) is studied. Results indicate a highly pulsed microdischarge with plasma densities of ~10^{19} m^{-3} and gas temperature excursions of ~ 150 K occurring in the discharge during the pulse. It is also seen that the dominant heating mechanism in these discharges are through ion Joule heating. Higher electron densities and spatially dominant thermal source terms are observed at 20 MHz excitation compared to the 10 MHz case. A specific impulse of 61 seconds was seen after power deposition for the 10 MHz case compared to cold gas specific impulse of 55 seconds. Higher specific impulse (65 seconds) is seen for the 20 MHz case compared to the 10 MHz case. The results validate the RF excited micro cavity discharge concept for electro-thermal microthruster applications.

7.0 EXPERIMENTAL RESULTS

7.1 Thrust Measurements

Thrust measurements were performed on the compact thrust stand following the procedure described in section 3.2.1. Since the initial set of thrusters had an integral supersonic nozzle, the initial measurements were focused on establishing the thrust coefficient of the nozzle. Before measurements could be taken, the linearity of the thrust stand first had to be confirmed. As detailed in Wilson and Burton(Wilson, et al., 1997), the compact thrust stand makes use of a precision jack-screw to produce precisely controlled small displacements. This known displacement value is used to generate a calibration curve, as seen in Figure 7.1. Following calibration of the LVDT, thrust coefficient measurements were obtained.

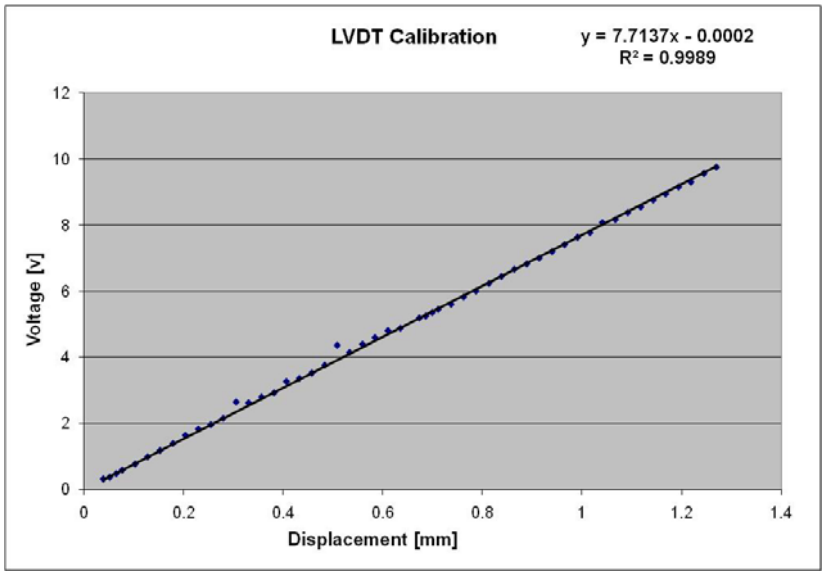

Figure 7.1: LVDT calibration curve for MCD thrust test runs. The correlation coefficient value (R^2) indicates a highly linear system.

The thrust coefficient of the integral supersonic nozzle is defined in equation (3.5) and repeated for convenience:

$$C_f \equiv \frac{T}{p_o^* A^*} \tag{7.1}$$

As noted in section 3.2.1, the effective throat area A^* is dependent on, among other factors, accurate knowledge of the mass flow rate. Early test runs with the MCD thruster were made with mass flow meters that were later found to be defective, which prohibited an accurate determination of the thrust coefficient. The decision was made to rely on the theoretical concepts and experimental results provided in Bayt (Bayt, 1999) and the one set of accurate data available. The accurate results obtained with the MCD thruster are shown below in Table 7.1 and Figure 7.2.

Table 7.1: Thrust Coefficient Testing Results

Line Pressure [kPa]	Mass Flow Rate [mg/s]	Thrust [mN]	C_f
120	0.99	0.60	1.26
240	5.22	2.70	1.07

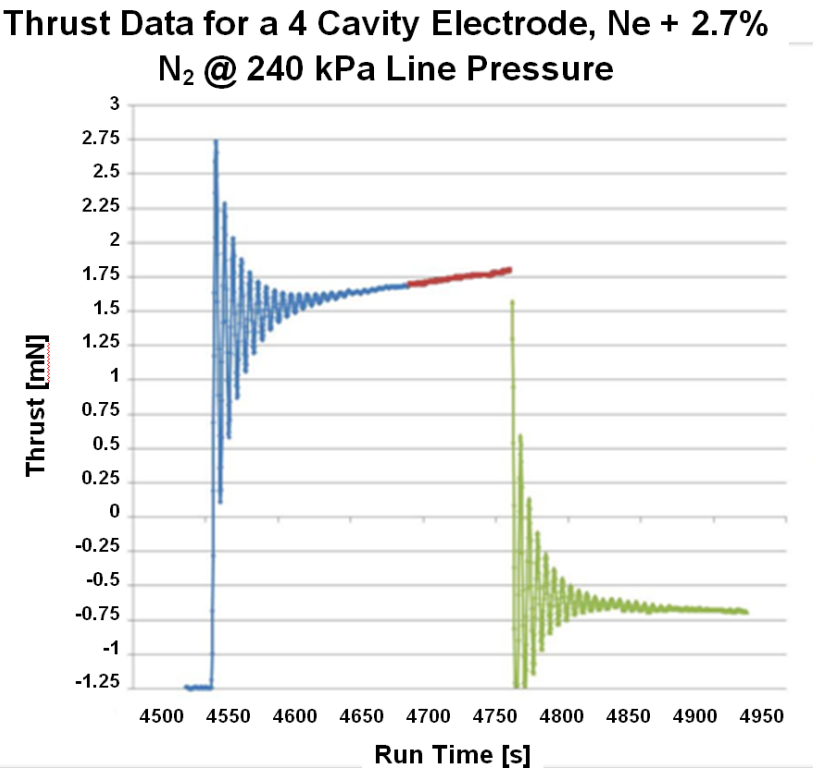

Figure 7.2: Thrust measurement for a 4 cavity electrode. Blue indicates the initial cold thrust state, red indicates the powered state, and green the final cold state. The cavity diameter is 120 µm widening to an exit diameter of 210 µm. The cavity nozzles are bell shaped with a 70 degree turn angle. This particular case is a constant thrust test at approximately 2.5 mN with a C_f of 1.07.

Even with the limited results available it is evident that the addition of a supersonic nozzle increases the thrust capability of the MCD thruster. The thrust coefficient of 1.26 observed in the 120 kPa case is consistent with theoretical results, although in the ideal case the turning angle would be greatly reduced. After validation of the supersonic nozzle, it was decided to omit the diverging nozzle from future thrusters for the sake of simplifying fabrication, although future operation thrusters will include contoured nozzles. For the sake of convenience the MCD thruster was moved to the smaller 0.15 m^3 vacuum tank for Paschen breakdown and thermal efficiency testing.

7.2 Paschen Breakdown Testing

Determination of the Paschen breakdown minimum was conducted in accordance with the procedure given in section 3.2.2. Paschen breakdown testing of the MCD thruster was initially intended to provide an estimate of the voltage required for thruster operation, but during testing the question of the appropriate pd parameter arose. In brief, for MCD devices intended for illumination, in which the cavity does not pass all the way through the electrode, the dominant electrode separation distance is in fact the diameter of the microcavity. (Park, et al., 2002) However, in the case of the MCD thruster using the cavity diameter as the electrode separation distance resulted in values that differed greatly from the DC breakdown curves given in Carazzettia et al. (Carazzettia, 2009) Once the pd characteristic was modified to use the separation

distance between the parallel foils the Paschen breakdown results fell in agreement with DC breakdown values, as shown in Figure 7.3 and described in de Chadenedes et al. (de Chadenedes, et al., 2010) When the cavity diameter is used in the pd characteristic, there is a stark contrast in the Paschen minimum between the MCD thruster and DC devices, illustrated in Figure 7.3. This result leads to the conclusion that for non-static MCD devices, the appropriate separation distance is the gap between the two parallel aluminum substrates.

Once the appropriate electrode separation distance was determined Paschen breakdown minimum values were obtained for the MCD thruster. Over the course of development, the thickness of the dielectric material has increased from 10 μm to 20 μm, and Paschen curves were obtained for both electrode configurations. The results for the 10 μm thick oxide layer (20 μm electrode separation distance) are seen in Figure 7.4 while those for the 20 μm thick oxide layer are seen in Figure 7.5. In order to run at optimal conditions, electrodes with the 20 μm thick oxide layer were all run at the same line pressure of 40 kPa, while the nitrogen content was varied. Thus Figure 7.5 describes the effect of nitrogen content on the Paschen minimum, while the shape of the Paschen curve remains the same as that described in Figure 7.4.

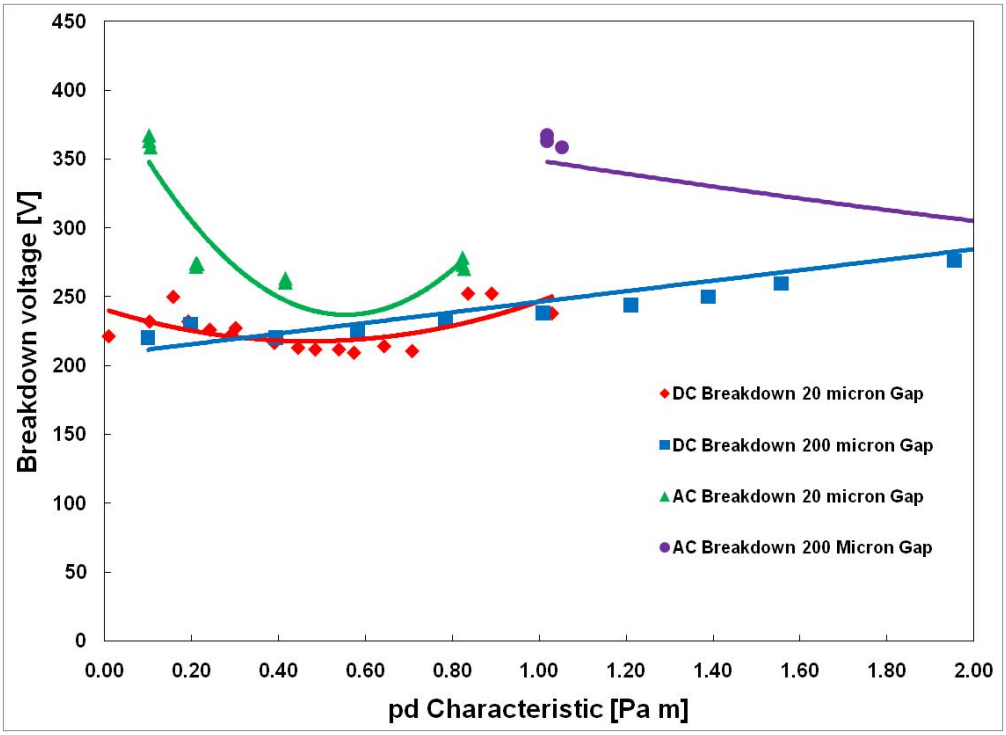

Figure 7.3: Paschen minimum breakdown characteristics of an MCD thruster (green and purple) and a DC device (red and blue). (Carazzettia, 2009) Using the 20 μm separation distance, the AC MCD thruster has a Paschen minimum at the same pd characteristic as the DC device, with a minor offset resulting from the addition of a dielectric layer to the MCD thruster. In the case of a 200 μm gap, the Paschen minimum of the MCD thruster occurs off the scale while the minimum of the DC device occurs at approximately 0.40 Pa m. Furthermore, the slope for the MCD thruster in the 200 μm case has a negative value as opposed to the DC device's positive value.

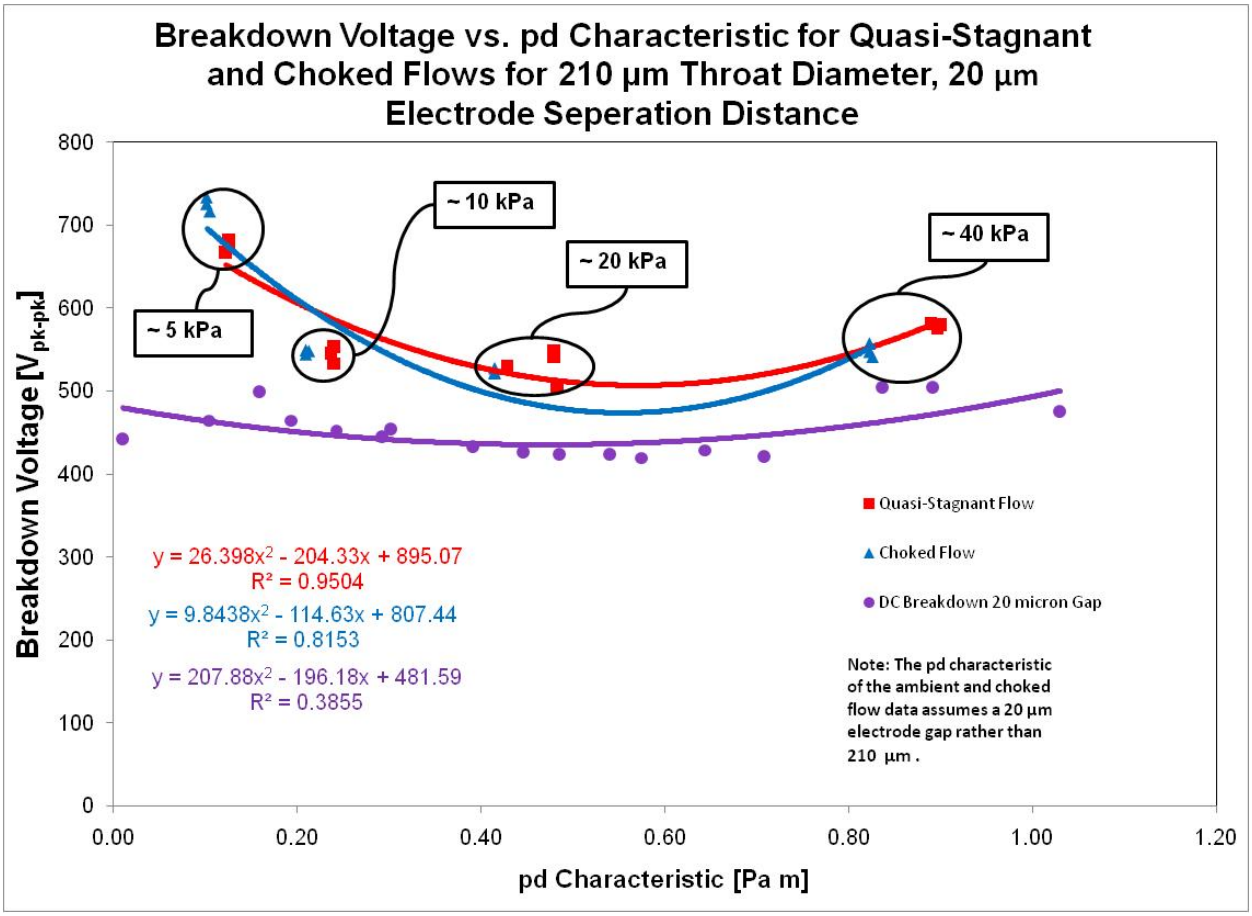

Figure 7.4: The Paschen breakdown minimum curve for a 20 µm electrode separation distance thruster. The red curve is quasi-stagnant, or near stationary flow, and the blue curve is choked flow. The Paschen minimum occurs at approximately the same pd characteristic as in the DC case, but the described curve is steeper and there is a voltage offset at the minimum due to the dielectric barrier effect of the aluminum oxide layer.

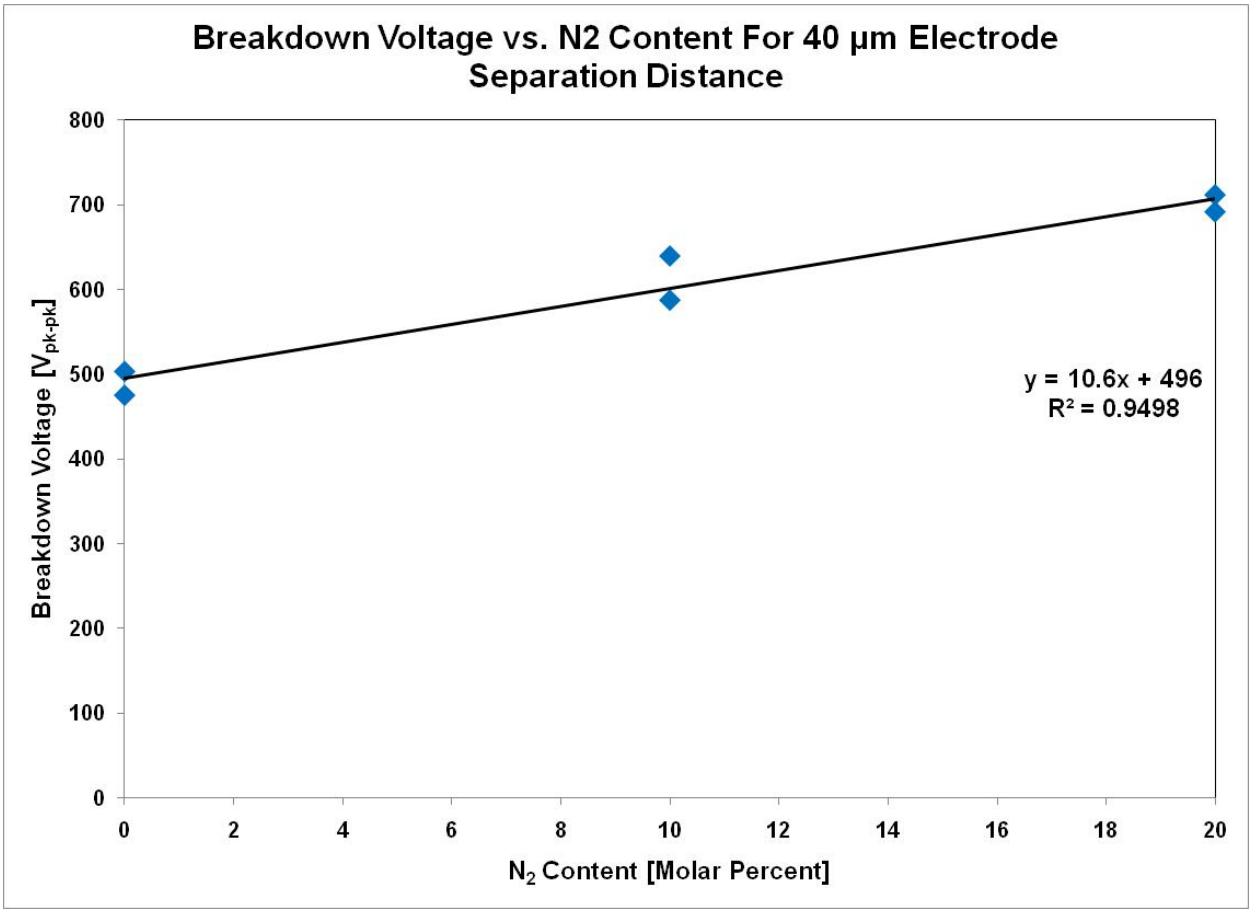

Figure 7.5: Paschen breakdown minimum voltage vs. N_2 content (as a molar ratio, not a mass ratio) for two thrusters with 40 µm electrode separation distance. The nominal pd characteristic is 1.6 Pa m.

From Figure 7.3 and Figure 7.4 it is clear that the MCD thruster exhibits Paschen minimum breakdown characteristics similar to those of a DC device. Since a new breakdown is initiated with each half-cycle in an approximately equivalent manner to a rising DC voltage, this result agrees with the theoretical expectations of the plasma formation mechanics occurring inside the microcavity. Additionally, Figure 7.5 illustrates the effect of an increased N_2 content on the breakdown voltage. As the Paschen minimum for Ar is lower than that of N_2 (Cobine, 1958), this result also agrees with theory. Therefore, although correction factors must be introduced for the dielectric barrier, it is acceptable to perform system-level calculations using DC Paschen breakdown minimum values.

7.3 Heating and Thermal Efficiency Measurements

Heating and thermal efficiency measurements were performed in accordance with the procedure detailed in section 3.2.3. During early phases of testing the input power was measured using the instantaneous values computed by the oscilloscope and transmitted to LabVIEW. It was later determined that due to instabilities in the waveform during discharge this method was unable to accurately resolve the actual input power which lead to inaccurate thermal efficiency values. This section will focus

on later results made with the more accurate power measurement procedure detailed in section 3.2.3.

The Paschen minimum breakdown testing detail in section 3.2.2 gives an accurate picture of the voltages required for thruster operation. It was determined that the optimal voltage setting for the MCD thruster was between 150% and 200% of the Paschen minimum for a given pd characteristic. Early testing revealed that the maximum peak to peak voltage that can be applied to the electrodes without arcing is approximately 1.2 kV. Examination of Figure 7.4 reveals that this restriction limits heating testing of the MCD thruster to a base line pressure of 40 kPa in order to avoid arcing at optimal heating conditions. Although lower line pressures would result in less strain on the electrode, this in turn reduces the throat Reynolds number to unacceptable levels. Therefore it is desirable to operate at the maximum pd characteristic that can be endured by the electrode, which is approximately 40 kPa in the current configuration.

With a suitable line pressure determined, the primary issue under investigation with regards to heating and thermal efficiency measurements is the determination of the optimal nitrogen content for the propellant gas mixture. An additional concern is ensuring that the thruster has the heating capability to offer improved thrust over the cold gas case, and so a target of 300 K for the difference between T_{o2} and T_{o1} was set. The test conditions are shown in Table 7.2. Three electrodes were used for testing, the geometry of the test electrodes is listed in Table 7.3.

Table 7.2: Heating and Thermal Efficiency Test Conditions

Line Pressure [kPa]	Nominal p d Characteristic [Pa m]	N_2 Content [%]
40	1.6	0, 10, 20

Table 7.3: Thruster geometries.

Thruster	Upstream Cavity Diameter [μm]	Throat Diameter [μm]	Area Ratio
MCD-121	365	300	1.48
MCD-122	350	280	1.56
MCD-124	340	290	1.37

Each thruster was tested with 0, 10, and 20% N_2 propellant gas. In order to limit the effects of electrode fatigue on the data, the order in which each propellant gas composition is tested is varied with each thruster. MCD-121 ran 20%, 10%, then 0%; MCD-122 ran 0%, 10%, then 20%; MCD-124 ran 10%, 20%, then 0%. The degree of heating was calculated both by the pressure ratio method (ideal flow) given in equation (3.7) and the Rayleigh flow method described in section 2.2.1. Results for the heating and thermal efficiency runs are given in Table 7.4, Figure 7.7, and Figure 7.8.

Table 7.4: Heating and Thermal Efficiency Testing Results. Tests conducted @ 25 kHz

Thruster	Propellant N_2 Content [%]	Ideal Flow ΔT_{o2} [K]	Rayleigh Flow ΔT_{o2} [K]	Ideal Flow η_{th} [%]	Rayleigh Flow η_{th} [%]
MCD-121	0	58.9	46.3	8.9	6.1
	10	124.6	96.8	14.8	11.5
	20	181.8	142.1	12.8	10.0
MCD-122	0	89.6	76.2	9.2	7.8
	10	121.0	103.3	10.7	9.1
	20	159.0	136.7	11.4	9.8
MCD-124	0	99.5	73.4	14.7	10.8
	10	94.5	63.6	7.5	5.5
	20	244.0	135.3	17.8	9.9

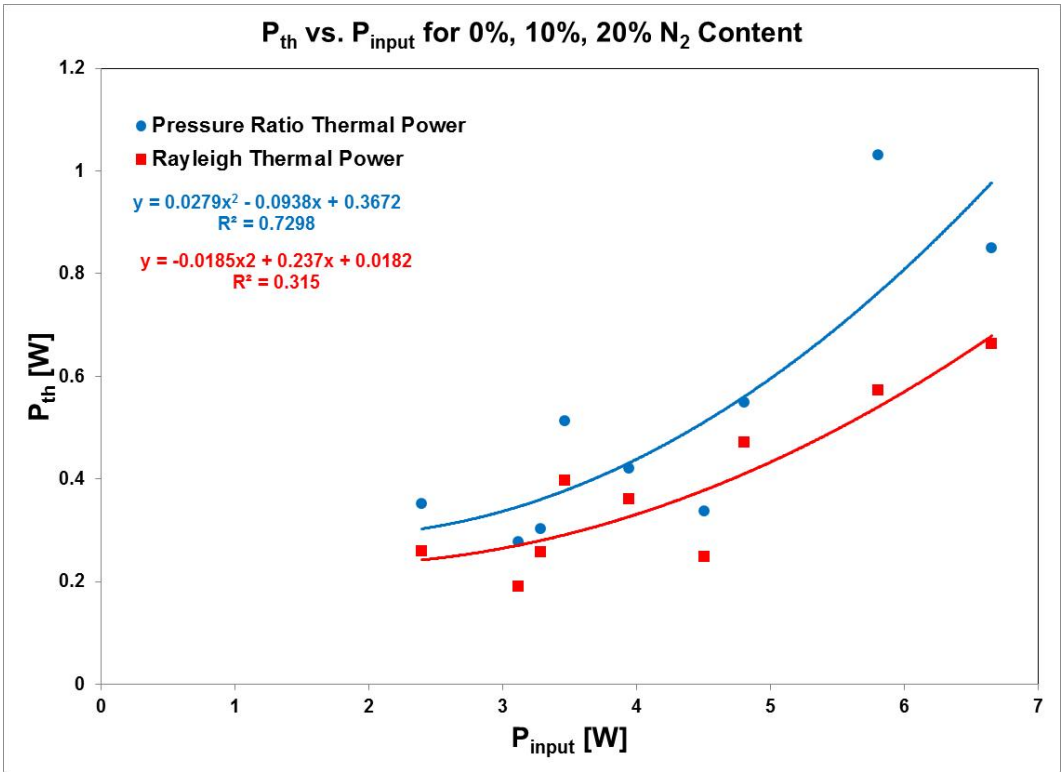

Figure 7.6: P_{th} as a function of P_{input} for the three test thrusters. Tests were conducted at 25 kHz.

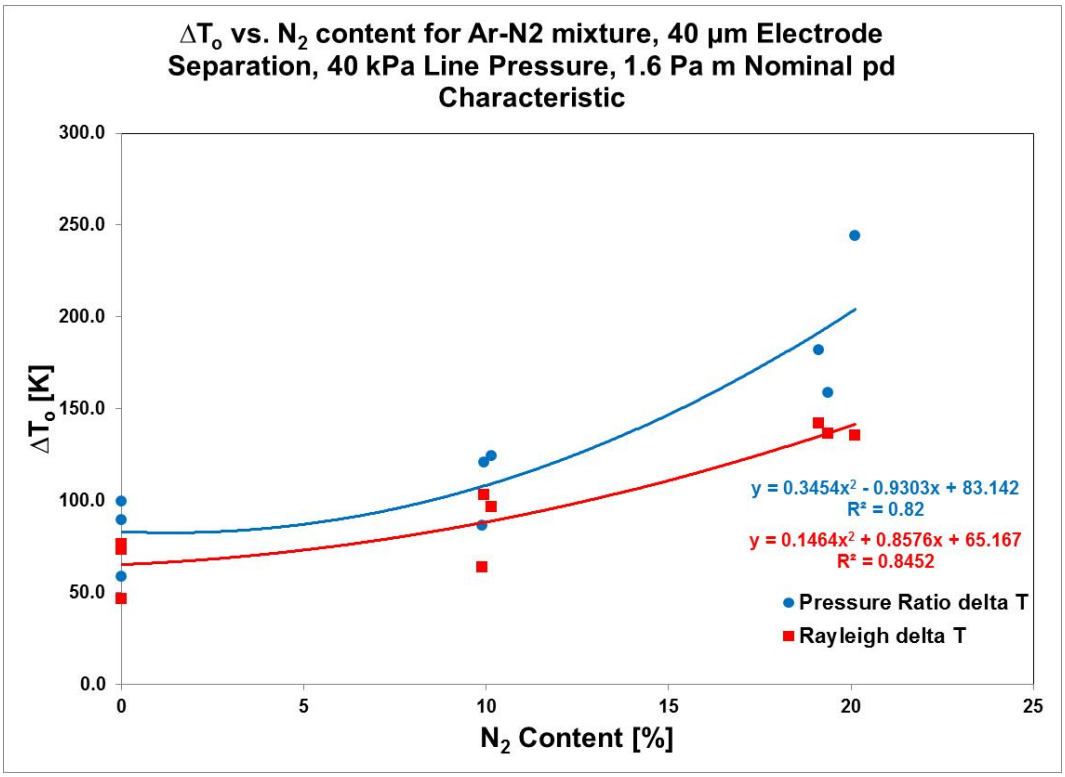

Figure 7.7: ΔT_o as a function of N_2 content for the three test thrusters. Tests were conducted at 25 kHz.

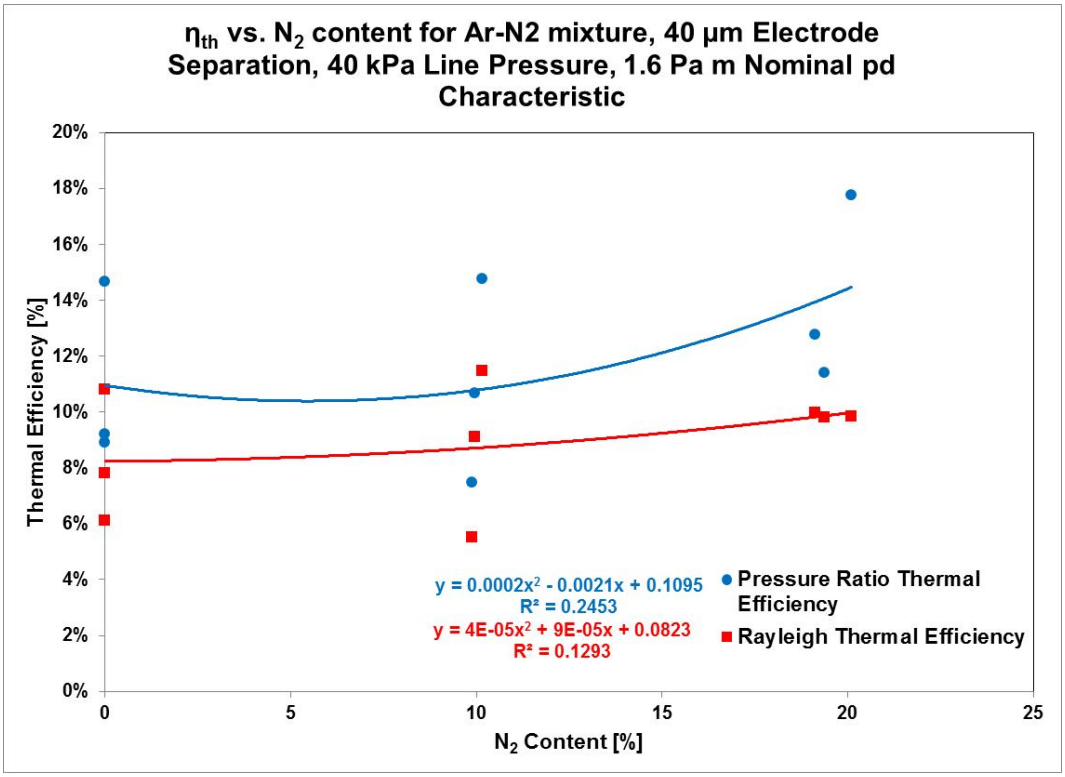

Figure 7.8: η_{th} as a function of N_2 content for the three test thrusters. Tests were conducted at 25 kHz.

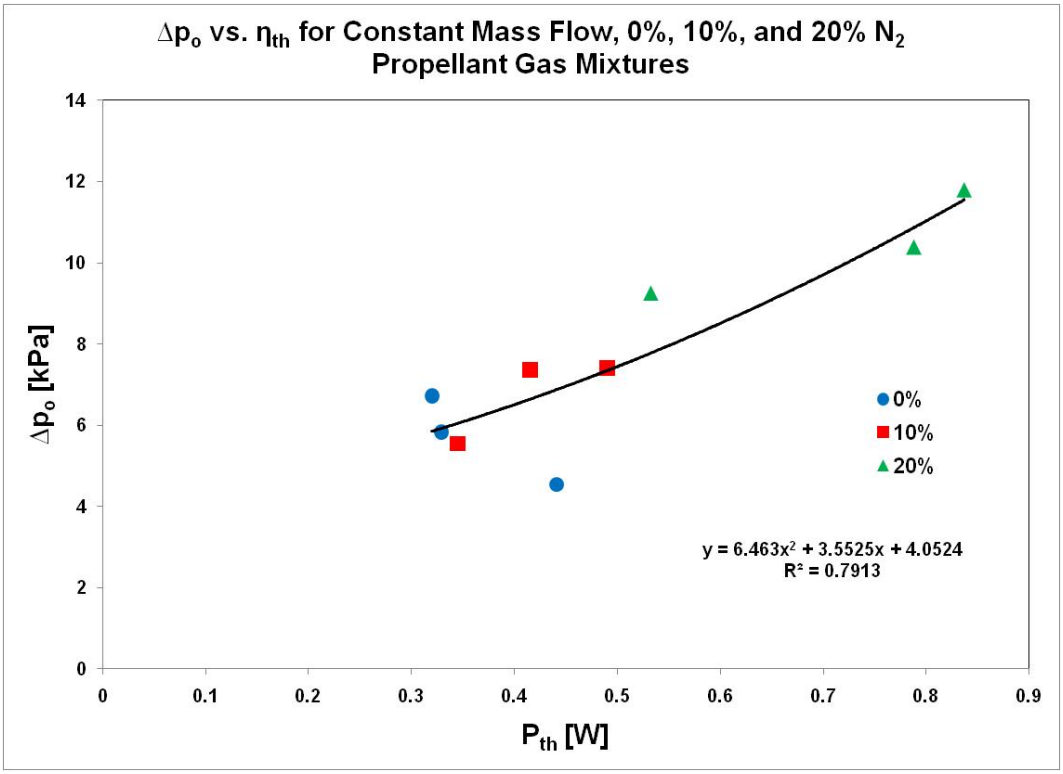

Figure 7.9: Δp_o as a function of P_{th} for the three test thrusters. Tests were conducted at 25 kHz.

Although these results were obtained at 25 kHz, additional runs were made at 50 and 100 kHz. In these additional tests, however, the discharge coefficient dropped significantly (10%) during testing, indicating damage to the cavity wall and dielectric layer which prevented significant results from being obtained. The effect of a higher frequency on heating and thermal efficiency is also discussed in Section 6.0.

Although not included in Table 7.4, one previous thruster did achieve a peak ΔT_o of 1075 degrees K at approximately 25% thermal efficiency as calculated by the ideal flow method. Unfortunately the thruster sustained significant damage to the cavity walls and dielectric layer as a result of the high temperatures (see Figure 7.10). Despite the failure of the electrode, this example does serve as an indication of the potential of the MCD thruster.

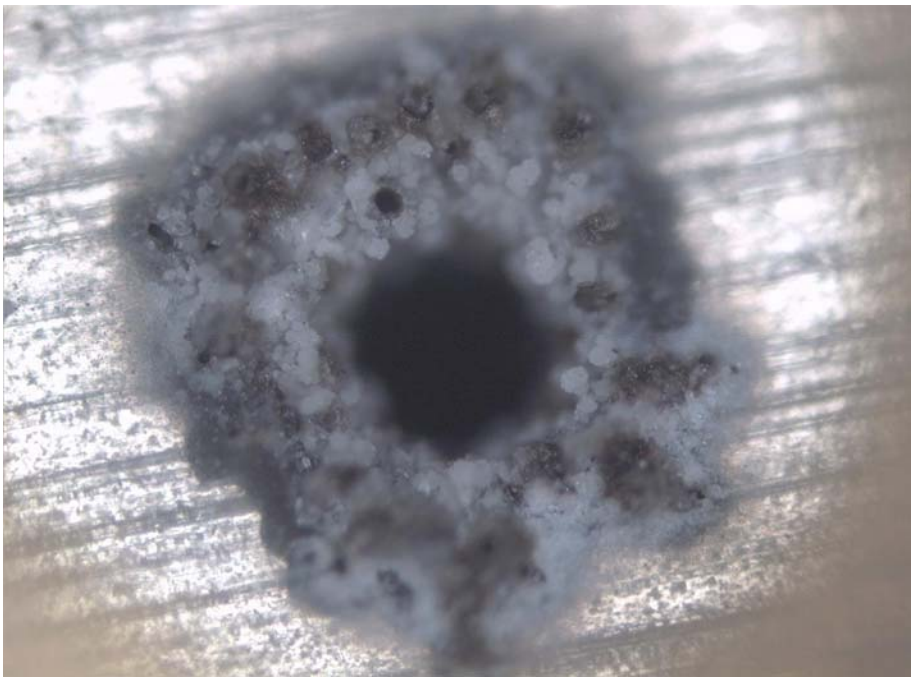

Figure 7.10: The effects of 1000 K ΔT_o bulk gas heating. The nanoporous alumina structure does not appear to be present.

7.3.1 Error Analysis

The error in the efficiency measurements can be determined by an analysis of the efficiency equation, repeated below:

$$\eta_{thermal} = \frac{\dot{m} C_p \Delta T_o}{P_{input}} \tag{7.2}$$

It is already known that the deviation of an input power measurement is 15% over 12 samples. The parameter ΔT_o is a quadratic function of the mass flow rate and cavity diameter, and a linear function of the pressure and discharge coefficient. The uncertainty of the mass flow sensors is ± 1.5%, the uncertainty of the pressure transducer is ± 0.25%, and the uncertainty of the cavity diameter is ± 0.8%. The additional mass flow parameter makes it a third order term in the calculation, while the specific heat is assumed to be constant. Since the discharge coefficient is a quadratic function of the pressure and a linear function of the mass flow rate, the overall uncertainty of the discharge coefficient is 1.5% by a propagation of errors calculation. Therefore, by a propagation of errors calculation the overall uncertainty in the thermal efficiency power measurement is 3.1%. When combined with the power measurement this results in a total uncertainty of 15.6%, indicating that the uncertainty in the power measurement is by far the dominant term.

8.0 CONCLUSION

8.1 Summary

A new trend in space exploration is the deployment of small-scale satellites known as nanosatellites. Nanosatellites have the potential to be an effective means of performing low-cost research and observation missions, but the lack of an effective, compact, and efficient propulsion system remains an obstacle. This work has focused on the exploration of the potential of microcavity discharge devices to serve in an electrothermal thruster role, especially in the case of nanosatellite propulsion. Microcavity discharge devices represent a new type of electronic device that was originally developed for use in plasma displays. An MCD device is a modified capacitor where one or more microcavities have been formed within each plate and then concentrically aligned to concentrate the capacitive fringe effects and magnify the electric field inside the cavity. MCD devices can be adapted to serve as thrusters by applying an AC voltage, causing the strong electric field inside the cavity to initiate plasma breakdowns, increasing the propellant gas temperature. Development of this electrothermal thruster, named the MCD thruster, has been conducted primarily on an experimental basis with computational modeling support. In order to validate the performance of the MCD thruster three sets of tests have been performed: thrust tests, Paschen minimum breakdown tests, and thermal efficiency tests.

Thrust tests were performed on a compact thrust stand and indicated that an integral micronozzle produced a thrust coefficient large enough to be effective from an efficiency standpoint. Paschen minimum breakdown tests determined that the correct distance to use in the Pd parameter was the linear separation distance between the aluminum substrates of the two electrode foils. This finding differs from MCD devices used for illumination where the cavity diameter is the dominant distance. Paschen testing also provided a practical limit on the line pressure used in testing and a rough system-level estimate of the voltages required to make optimal use of the thruster. Heating and thermal efficiency testing indicated the MCD thruster was capable of a high degree of heating and moderate thermal efficiency, up to 280 K and 22%. Increased nitrogen content in the propellant gas generally increased the degree of heating and efficiency observed, due to two factors. First, in the MCD process nitrogen is a more effective energy absorbing agent, as the energy imparted by a collision is stored in the rotational and vibrational excited states in addition to the electronic excited state, and as a result greater energy is deposited in the propellant gas. Second, the addition of nitrogen to the propellant gas results in the majority of the heating occurring away from the cavity walls, reducing wall heat losses and increasing the thermal efficiency.

Although the current generation of MCD thrusters is limited due to material choices and fabrication processes, they are still capable of a relatively high level of performance. The optimal operating conditions, as determined by the maximum thermal efficiency and the resulting heating and efficiency are found to occur with a mixture of argon-15% nitrogen, for which a constant mass flow rate with heating resulted in a pressure increase of 50 - 75%, and a corresponding stagnation temperature increase of 125 – 200%.

Table 8.1: Estimated optimal operating conditions and performance figures for a single cavity thruster with Ar-N_2 propellant gas.

Line Pressure [kPa]	N_2 Content [%]	Δp_o [kPa]	ΔT_o [K]	η_{th} [%]
40	15	30	500	25
100	15	50	300	35

8.2 Recommendations and Future Work

This work covered the earliest stages of development of the MCD thruster. The possibilities for future work are vast. Two additional projects utilizing MCD thruster technology are underway. The first is an improved CFD model of the MCD discharge process being undertaken at the University of Texas at Austin. The second effort is the use of a modified MCD thruster as a means of dissociating gaseous iodine for a gas-dynamic laser being undertaken at the High Energy Laser Lab at the University of Illinois. Further development of MCD devices for use as spacecraft thrusters can proceed in many directions. From both a system and an efficiency standpoint the argon-nitrogen mixture currently used as a propellant is non-optimal and a number of different substances are candidates for further exploration. Initial studies of storable liquid propellants such as nitrous oxide and various refrigerants have been performed. From a systems perspective liquid propellants are a more attractive option than pressurized gasses, as they have a higher storage density and a smaller tankage fraction. Within the Ar-N_2 system currently in use the optimal propellant mixture remains to be determined and efforts to maximize efficiency simply by altering the nitrogen content would be of great benefit to the overall system integration of the thruster. Perhaps the most immediate concern is the improvement of the materials used in fabrication of the electrode foils, as the current aluminum/aluminum oxide system has several limitations with respect to system robustness.

The ultimate goal of any thruster project is of course operational deployment on a spacecraft, and the MCD thruster is no exception. Since the MCD thruster has a number of advantages with respect to nanosatellite use, it remains a candidate for use on several proposed Cube Sat missions. As with any propulsion system, the thruster configuration would have to be modified to meet system parameters, but it is likely that such efforts would show that the MCD thruster will be ideally suited for the role of nanosatellite propulsion.

9.0 REFERENCES

Anderson J. D. [Book Section] // Modern Compressible Flow With Historical Perspective, Third Edition. - New York : McGraw-Hill, 2004.

Baker Adam M., Da Silva, Curiel A., Schaffner, J., Sweeting, M. You Can Get There From Here: Advanced Low Cost Propulsion concepts for Small Satellites Beyond LEO [Journal] // Acta Astronautica. - 2005. - 2-8 : Vol. 57. - pp. 288-301.

Bayt Robert L. Analysis, Fabrication, and Testing of a MEMS-based Micropropulsion System [Report] : PhD Thesis / Massachusetts Institute of Technology. - Cambridge, MA : [s.n.], 1999.

Becker K. H., Schoenbach, K. H., Eden, J. G. Microplasmas and Applications [Journal] // Journal of Physics D: Applied Physics. - 2006. - 3 : Vol. 39. - pp. R55-R70.

Bitzer D. L., Slottow, H. G. The Plasma Display Panel- A Digitally Addressable Display With Inherent Memory [Conference] // Proceedings of the American Federation of Information Processing Societies. - Washington, D.C. : [s.n.], 1966. - p. 541.

Burton R. L. [et al.] Development of the MCD Thruster for Nanosat Propulsion [Conference] // Proceedings of the 57th Joint Army Navy NASA Air Force Propulsion Meeting. - Colorado Springs, Colorado : [s.n.], 2010.

Burton R. L., et al Initial Development of the Microcavity Discharge Thruster [Conference] // Proceeding of the 31st Internation Electric Propulsion Conference. - Ann Arbor, Michigan : [s.n.], 2009.

Carazzettia P., Renaudb, Ph., Shea, H. R. Experimental Study of Electrical Breakdown in MEMS Devices With Micrometer Scale Gaps [Journal] // Proceedings of SPIE (International Society for Optics and Photonics). - 2009. - Vol. 6884. - pp. 688404-1-11.

Cartwright D. C., Trajmar, S., Chutjian, A., Williams, W. [Journal] // Physical Review A. - 1977. - 3 : Vol. 16. - pp. 1041-1051.

Cengel Y. A., Cimbala, J. M. [Book Section] // Fluid Mechanics: Fundamentals and Applications. - New York : McGraw-Hill, 2004.

Cobine J. D. Gaseous Conductors: Theory and Engineering Applications [Book]. - New York : Dover Publications, 1958. - 1st Edition.

Cubesat Program California Polytechnic State University [Online] // Cubesat Design Specification Rev. 12. - August 2009. - http://cubesat.atl.calpoly.edu/images/developers/cds_rev12.pdf.

de Chadenedes M. [et al.] Advances in Microcavity Discharge Thruster Technology [Conference] // Proceedings of the 46th AIAA/ASME/SAE/ASEE Joint Propulsion Conference. - Nashville, TN : [s.n.], 2010.

Deconinck T. Simulation Studies of Direct-current Microdischarges for Electric Propulsion [Report] : Ph.D. Dissertation / Department of Aerospace Engineering and Engineering Mechanics ; UT Austin. - Austin, TX : [s.n.], 2008.

Deconinck T., Mahadevan, S., and Raja, L. L. Computational simulation of coupled nonequilibrium discharge and compressivle flow phenomena in a microplasma thruster [Journal] // Journal of Applied Physics. - 2009. - Vol. 106. - pp. 063305 1-13.

Deconinck T., Raja, L. L. [Journal] // Plas. Proc. Polym.. - 2009. - Vol. 6. - pp. 335-346.

Fife J. M. [et al.] Orbital Performance Measurements of Air Force Electric Propulsion Space Experimental Ammonia Arcjet [Journal] // Journal of Propulsion and Power. - 2002. - 4 : Vol. 18. - pp. 749-753.

Ghosh Alexander M. Study of Atmospheric Drag Recovery Trajectories of Low-thrust Cubesats [Report] : Masters Thesis / University of Illinois at Urbana Champaign. - Urbana, IL : [s.n.], 2009.

Goovaerts K. M., Bilen S. G. and Micci M. M. Design and Initial Testing of Miniature Microwave Electrothermal Thruster (MiniMET) [Journal]. - 2007. - AIAA Paper 2007-5293.

Lichon P. G., Tilley, D. L., Anderson, R., Sankovic, J. M. 500 W Arcjet System Development and Demonstration [Conference] // Proceedings of the 26th International Electric Propulsion Conference. - 1997. - IEPC-97-088.

Mahadevan S, Raja, L. L. [Journal] // Journal of Applied Physics. - 2010. - 9 : Vol. 107. - pp. 093304 1-11.

Moravej M. et al [Journal] // Plasma Sources Sci. Technol.. - 2006. - Vol. 15. - pp. 204-210.

Morren W. E., Hay, S. S., Haag, T. W., Sovey, J. S. Performance Characterizations of an Engineering Model Multipropellant Resistojet [Journal] // Journal of Propulsion and Power. - 1989. - 2 : Vol. 5. - pp. 197-213.

Park S-. J. [et al.] Microdischarge Arrays: A New Family of Photonic Devices (Revised) [Journal] // IEEE Journal on Selected Topics in Quantum Electronics. - March/April 2002. - 2 : Vol. 8. - pp. 387-394.

Phelps A. V., Pitchford, L. C. [Journal] // Physical Review A. - 1985. - 5 : Vol. 31. - pp. 2932-2949.

Physics of Electric Propulsion [Book Section] / book auth. Jahn R. G.. - New York : McGraw-Hill, 1968.

Shin J., Raja, L. L. [Journal] // J. Appl. Phys.. - 2003. - 12 : Vol. 94. - pp. 7408-7415.

Sitaraman H., Raja, L. Simulation Studies of Alternating-Current Microdischarges for Microthruster Applications [Conference] // Proceedings of the 48th AIAA Aerospace Sciences Meeting, AIAA-2010-231. - 2010.

Slottow H. G. Plasma Displays [Journal] // IEEE Transactions on Electron Devices. - 1976. - Vol. 23. - pp. 760-722.

Spence D., Demmons N. and Roy T. A Compact Low-Power High-Isp Thruster for Microsatellites [Report] / Busek, Airforce Research Laboratory. - 2008. - AFRL-RZ-ED-TP-2008-233.

Takao Y., Eriguchi K. and Ono K. A Miniature Electrothermal Thruster Using Microwave-excited Microplasmas: Thrust Measurement and its Comparison With Numerical Analysis [Journal] // Journal of Applied Physics. - 2007. - Vol. 101. - pp. 123307-123316.

Thomas R. Development and Testing of a Gallium Electromagnetic (GEM) Thruster [Report] : PhD Thesis / University of Illinois at Urbana-Champaign. - Urbana, IL : [s.n.], 2010.

Vincenti W. G., Kruger, C. H. Introduction to Physical Gas Dynamics [Book]. - New York : Wiley, 1965.

Warner N. Z. and Martinez-Sanchez M. Design and Preliminary Testing of a Miniaturized TAL Hall Thruster [Conference] // Collection of Technical Papers-Proceedings of the AIAA/ASME/SAE/ASEE 42nd Joint Propulsion Conference. - 2006. - pp. v. 8, p. 6422-6435.

Watts Barry D. The Military Use of Space: A Diagnostic Assessment [Report] / The Center for Strategic and Budgetary Assessments. - Washington, D.C. : [s.n.], 2001.

Wilson M. J., Bushman S. S. and Burton R. L A Compact Thrust Stand for Pulsed Plasma Thrusters [Conference] // Proceedings of the 26th International Electric Propulsion Conference. - 1997. - pp. 765-772.

Yuan X. Raja, L. L. [Journal] // IEEE Trans. on Plasma Science. - 2003. - 4 : Vol. 31. - pp. 495-503.

APPENDIX A- THRUSTER AND ELECTRODE FABRICATION

All MCD thrusters tested were fabricated at the Laboratory for Optical Physics and Engineering at the University of Illinois. At the current level of technology the MCD thruster is assembled almost entirely by hand. Although there are several additional pieces involved, the key components of the MCD thruster are the two aluminum/aluminum oxide electrodes which form the plates of the capacitor. Fabrication of the electrodes is an involved process which will be described in brief below. Note that in order to protect intellectual property several steps have been omitted or edited.

1. The base material for the electrode is a 0.75" x 3" foil cut from 127 μm thick, 99% pure Aluminum (Al 1100) sheet.
2. The cavities are drilled into the base foil using a 100-300 μm diameter drill bit.
3. Burrs and deformations in the cavity are removed using an electro-polishing process with a perchloric acid and ethyl alcohol mixture.
4. The aluminum oxide dielectric layer is grown on the aluminum substrate via an 8-12 hour anodization process in an oxalic acid solution.
5. One of two cavity insulation material is added to block arcing between any cracks in the oxide layer that may form. Depending on the insulation material, different curing temperatures are used.
    a. Liquid polyimide is applied to the cavity via a spin-coating process and cured at 250 °C for 1 hour.
    b. A glass paste coating is applied to the cavity via a spin coating process and cured at a maximum temperature of 560 °C.
6. Once the insulation material has cured the electrodes are ready for assembly.

Following fabrication of the electrodes the two foils are aligned under a microscope, with the addition of a 25 μm thick polyimide insulation sheet if necessary. The electrode alignment is then secured with Loctite Hysol 1-C epoxy resin. The power wires are secured to an exposed portion of the aluminum substrate with conductive epoxy. A boron nitride discharge shroud is placed around the cavity exit to prevent arcing between the exhaust plume and the small exposed area of the downstream foil. A ¼" diameter glass tube is fitted over the discharge shroud so that the thruster can be connected to the Ultra Torr fitting on the vacuum tank. Finally, a ¼" diameter propellant feed tube is connected to the upstream side of the thruster and the whole assembly is covered in more Hysol 1-C resin to provide insulation.